

## Article

# Origin of Himalayan Eocene Adakitic Rocks and Leucogranites: Constraints from Geochemistry, U-Pb Geochronology and Sr-Nd-Pb-Hf Isotopes

Hang Liu<sup>1,2</sup>, Wenchang Li<sup>2,3,\*</sup>, Huawen Cao<sup>1,3,\*</sup> , Xiangfei Zhang<sup>1,2</sup>, Yang Li<sup>1</sup> , Ke Gao<sup>2</sup>, Lei Dong<sup>2</sup>, Kai Zhang<sup>2,4</sup> and Xin Liu<sup>2,4</sup>

<sup>1</sup> College of Earth Sciences, Chengdu University of Technology, Chengdu 610059, China; lhcdut1227@163.com (H.L.); zhangfei1895@163.com (X.Z.); liyangcdut@163.com (Y.L.)

<sup>2</sup> Chengdu Center (Geosciences Innovation Center of Southwest China), China Geological Survey, Chengdu 610218, China; gaokely@163.com (K.G.); donglei890712@126.com (L.D.); ozxkyzo@gmail.com (K.Z.); flyingliu0606@163.com (X.L.)

<sup>3</sup> College of Land and Resources Engineering, Kunming University of Science and Technology, Kunming 650093, China

<sup>4</sup> College of Earth Resources, China University of Geosciences, Wuhan 430074, China

\* Correspondence: lwcyndd@163.com (W.L.); caohuawen1988@126.com (H.C.)

**Abstract:** Within the Himalayan collisional belt, granites occur along two subparallel belts, namely, the Tethyan Himalayan Sequence (THS) and the Greater Himalayan Crystalline Complex (GHC). In this study, Eocene adakitic rocks and leucogranite are found only in the northern Himalayas, so further research is required to constrain their origin. Here, we present zircon U–Pb and monazite U–Th–Pb ages, Sr–Nd–Pb and Hf isotopes, and whole-rock major and trace elements for Liemai muscovite granite in the eastern Himalayan region. The U–(Th)–Pb results show that Liemai muscovite granite was emplaced at 43 Ma, and that its geochemical characteristics are similar to those of adakitic rocks of the same age (Dala, Quedang, Ridang, etc.). Combined with previous studies, both Eocene adakitic rocks and leucogranite are high-potassium calc-alkaline peraluminous granites. The former is relatively rich in large-ion lithophile elements (LILEs), such as Ba and Sr, and relatively deficient in high-field-strength elements (HFSEs), such as Nb, Ta, Zr, and Y, with weak or no Eu anomalies, and the average light rare earth element (LREE)/heavy rare earth element (HREE) ratio is 17.8. The latter is enriched in LILEs (such as Rb) and U, Ta, and Pb, and depleted in HFSEs (such as Nb and Zr), La, and Nd, with obvious negative Sr, Ba, and Eu anomalies and a mean LREE/HREE ratio of 10.7. The  $^{87}\text{Sr}/^{86}\text{Sr}$  of the former is in the range of 0.707517–0.725100,  $\epsilon\text{Nd}(t)$  ranged from  $-1.2$  to  $-14.7$ , the average is  $-11.6$ ,  $\epsilon\text{Hf}(t)$  ranged from  $-0.5$  to  $-65$ , the average is  $-12.2$ . The average values of  $(^{206}\text{Pb}/^{204}\text{Pb})_i$ ,  $(^{207}\text{Pb}/^{204}\text{Pb})_i$  and  $(^{208}\text{Pb}/^{204}\text{Pb})_i$  are 18.788, 15.712 and 39.221, respectively; The  $^{87}\text{Sr}/^{86}\text{Sr}$  of the latter is in the range of 0.711049–0.720429,  $\epsilon\text{Nd}(t)$  ranged from  $-9.8$  to  $-13.8$ , the average is  $-12.3$ ,  $\epsilon\text{Hf}(t)$  ranged from  $-4.2$  to  $-10$ , the average is  $-6.7$ . The isotopic characteristics indicate that adakitic rocks and leucogranites are derived from the ancient lower crust, and both may be derived from metamorphic rocks of the GHC. In this paper, the origin of the two is associated with the transformation of the Himalayan tectonic system during the Eocene, and it is inferred that the deep crust may have altered the tectonic environment (temperature and pressure), resulting in an obvious episodic growth trend of leucogranite and significant development of adakitic rocks from 51 to 40 Ma. From 40 to 35 Ma, the development of Eocene magmatic rocks was hindered, and adakitic rocks disappeared. It is proposed that the genetic difference is related to the transition from high to low angles of the subducting plate in the crustal thickening process.

**Keywords:** Himalaya; Eocene; adakitic rocks; leucogranites; Liemai; origin



**Citation:** Liu, H.; Li, W.; Cao, H.; Zhang, X.; Li, Y.; Gao, K.; Dong, L.; Zhang, K.; Liu, X. Origin of Himalayan Eocene Adakitic Rocks and Leucogranites: Constraints from Geochemistry, U-Pb Geochronology and Sr-Nd-Pb-Hf Isotopes. *Minerals* **2023**, *13*, 1204. <https://doi.org/10.3390/min13091204>

Academic Editor: Alexandre Andronikov

Received: 12 August 2023

Revised: 6 September 2023

Accepted: 7 September 2023

Published: 13 September 2023



**Copyright:** © 2023 by the authors. Licensee MDPI, Basel, Switzerland. This article is an open access article distributed under the terms and conditions of the Creative Commons Attribution (CC BY) license (<https://creativecommons.org/licenses/by/4.0/>).

## 1. Introduction

In the Tethyan Himalayas regime, a belt of leucogranites up to 2000 km long is distributed approximately along the east–west direction, nearly parallel to the Greater and northern Himalayas. They are important rock probes for studying the tectonic–magmatic evolution history of the Himalayan orogenic [1–9]. Therefore, the detailed study of leucogranite is very important for determining the evolution of the Himalaya–Tibetan Plateau orogenic belt [7,10–14].

In addition to Eocene leucogranite, Eocene adakitic rock associated with thickening crust has been found in the northern Himalayan region by previous scholars. These discoveries have aroused widespread attention among experts and scholars at home and abroad, and the discussion has focused on the genesis, metamorphism, and tectonic evolution mechanism [11,12,15–22]. However, there are different understandings regarding the origin of adakitic rocks. Gao et al. (2021b) [20] used the fractional crystallization model to invert the differentiation and evolution process between Eocene two-mica granite (heap crystal) and Eocene leucogranite, indicating that adakitic rock with a high Sr/Y ratio may be formed via fractional crystallization. However, Zeng et al. (2011, 2014) [10,11] found that the middle Eocene high-Sr/Y adakitic granites in the northern Himalayan gneiss dome originated from the thickened lower crust. Xie et al. (2010) [15] and Dai et al. (2020) [22] proposed that Dala two-mica granite has an affinity for adakitic rocks and is the product of the partial melting of deep rocks dominated by garnet and amphibole under high pressure. Hou et al. (2012) [23] and Cao et al. (2020) [24] reported that the oceanic crust plates of the Neo-Tethys Ocean broke off at 45 Ma, after which a brief extension occurred in the northern Himalayas from 45 to 40 Ma, resulting in large amounts of adakitic rocks. Tian et al. (2017) [25] and Dai et al. (2023) [21] stated that Liemai two-mica granite and muscovite granite are the products of the partial melting of metamorphic rocks in a thickened crustal environment. In the latest study of Cao et al. (2022) [6], the genesis of Cenozoic leucogranite was investigated in detail. Their team proposed that the Himalayan leucogranite originated from the inconsistent (unbalanced) partial melting of the Greater Himalayas complex and experienced highly differentiated evolution of mineral separation and crystallization. However, no systematic comparative study has been conducted to determine the differences and genetic connections between Eocene adakitic rock and leucogranite in the northern Himalayas. In this study, it was found that Eocene adakitic rocks and leucogranites are exposed only in the northern Himalayas (Supplementary Table S1) and are mainly concentrated in the dome structure of the eastern part of the northern Himalayas. These two types of granites exhibit obvious differences in their spatial and temporal distribution and geochemical characteristics. On this basis, previous studies on adakitic rocks and leucogranites in this area were reviewed [10,19,23,26–32].

To comprehensively determine the genesis and tectonic evolution characteristics of these two types of Eocene granite, we focused on the Eocene northern Himalayas and investigated Liemai muscovite granite. Zircon and monazite U–(Th)–Pb dating, whole-rock major and trace element analysis, and Sr, Nd, Pb, and Hf isotope analyses were conducted. At the same time, the genesis (partial melting and fractional crystallization) and diagenetic constraints (temperature, pressure, depth, etc.) of the considered leucogranite were related to the transformation of the Himalayan Eocene tectonic system, with the aim of exploring and constraining the genetic mechanism of granite in the collisional orogenic belt.

## 2. Geological Background

The Qinghai–Tibetan Plateau, which has experienced a long, multistage and complex history of oceanic spreading, subduction and continental collision, consists of the Songpan-Ganzi, North Qiangtang, South Qiangtang, Lhasa and Himalayan (Indian) blocks, from north to south [33,34]. The Himalayan orogenic belt was formed by the continental collision between the Indian and Eurasian blocks [33–35]. The orogen is separated from the Lhasa block in the north by the Yarlung Tsangpo suture zone, and from the Indian block in the south by the Main Frontal Thrust. Four major tectonic units have been defined

from north to south—the Tethyan Himalayan Sequence (THS, also referred to as northern Himalaya), the Greater Himalayan Crystalline Complex (GHC), the Lesser Himalayan Sequence (LHS), and the Sub-Himalayan Sequence (SHS)—which are separated by the South Tibet Detachment System (STDS), the Main Central Thrust (MCT) and the Main Boundary Thrust (MBT), respectively [2,35] (Figure 1). In the northern Himalayan tectonic belt, a series of gneiss domes developed, known as northern Himalayan gneiss domes (NHGDs). The core of the NHGDs comprises gneiss and leucogranite overlying a layer of non-metamorphic sedimentary rocks transitioning to high-grade metamorphic clastic rocks [36]. The THS contains passive continental margin sedimentary rocks of the Indian block deposited during the Paleozoic–Mesozoic and mainly encompasses clastic and carbonate rocks metamorphosed under low-grade greenschist- and low-grade amphibolite-facies conditions [37]. The GHC represents the core of the Himalayan orogenic belt, which comprises Proterozoic–early Paleozoic sedimentary sequences and magmatic rocks. The GHC experienced granulite to eclogite-facies metamorphism, forming crystalline complexes that largely include schist, paragneiss, orthogneiss, amphibolite, marble, and granulite [38]. The Cenozoic magmatic rocks of the Himalayas primarily comprise leucogranite formed after continental–continental collision between the Indian and Lhasa blocks [6,39].

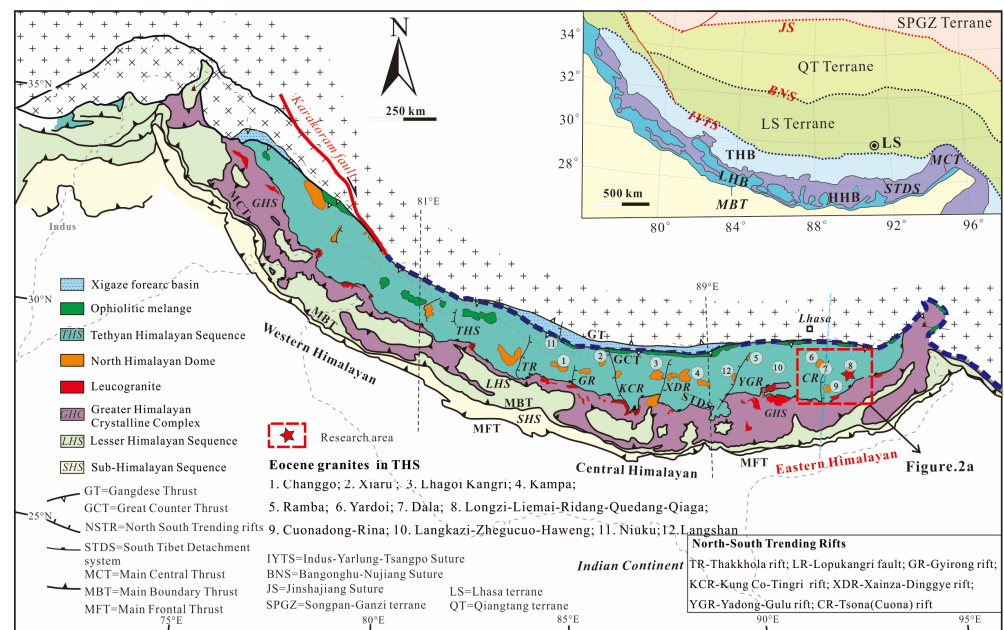


**Figure 1.** Age summary of Eocene magmatic rocks in the Himalayas. The map was modified from Cao et al. (2022) [6].

### 3. Sampling and Petrography

In this paper, five fresh muscovite granite samples were collected near the Longzi fault zone (longitude and latitude:  $92^{\circ}35'27.88''$  E and  $28^{\circ}27'14.02''$  N, respectively) in Yangxiong Village, Eastern Liemai Township, Longzi County, Shannan City, Tibet (Figure 2a). The mineral assemblages in Liemai muscovite granite do not exhibit a directional structural arrangement (Figure 2d), and some chloritization alteration and structural deformation are apparent, indicating that only brittle deformation occurs in Liemai muscovite granite. The contact boundary between the Liemai rock mass and wall rock is obvious. The wall rock of Liemai muscovite granite is medium–thick-layered light metamorphic sandstone and siltstone with dark gray silty slate in the second member of the Ridang Formation (Figure 2b). At the edge of the rock mass, muscovite granite mainly occurs as veins and interspersed in the wall rock. The width of the rock vein ranges from 1 to 2 m (Figure 2c), and the length of the rock vein ranges from approximately 100 to 500 m. A small amount

of muscovite granite exists in the form of rock plants and branches, and the exposed area is smaller than 1 km<sup>2</sup>.

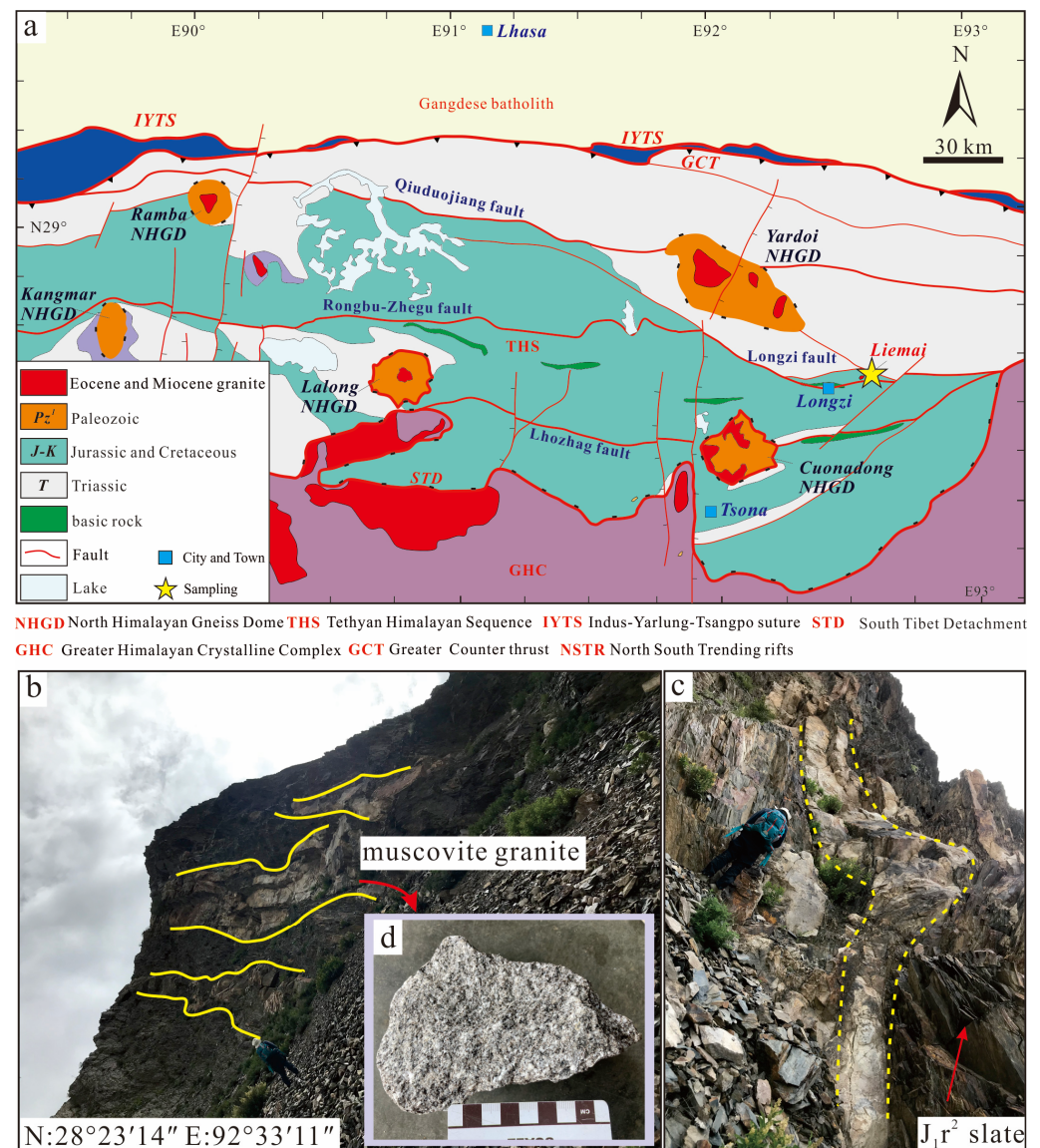


**Figure 2.** Sampling location map: (a) regional geological map of the study area modified from Cao et al. (2023a) [7]; (b–d) representative field photos and photos of Liemai muscovite granite samples.

The fresh rock surface exhibits an obvious porphyritic-like structure, which mainly includes quartz (2 vol. %), plagioclase (4 vol. %), and muscovite (5 vol. %). Plagioclase is of the self-shaped plate-columnar type (Figure 3b,c), muscovite is of the semi-self-shaped flake type, and quartz is of the other-shaped granular type. The matrix is a fine-grained granite structure, mainly comprising quartz (40%), muscovite (25 vol. %), K-feldspar (10 vol. %), plagioclase (10 vol. %), and biotite (4 vol. %) (Figure 3). Plagioclase and K-feldspar are of the semi-automorphic plate-columnar type, and some plagioclases contain obvious zoning structures (Figure 3b–d). Muscovite is scaly, quartz is anhedral granular, and the accessory minerals include apatite, zircon, and titanite.

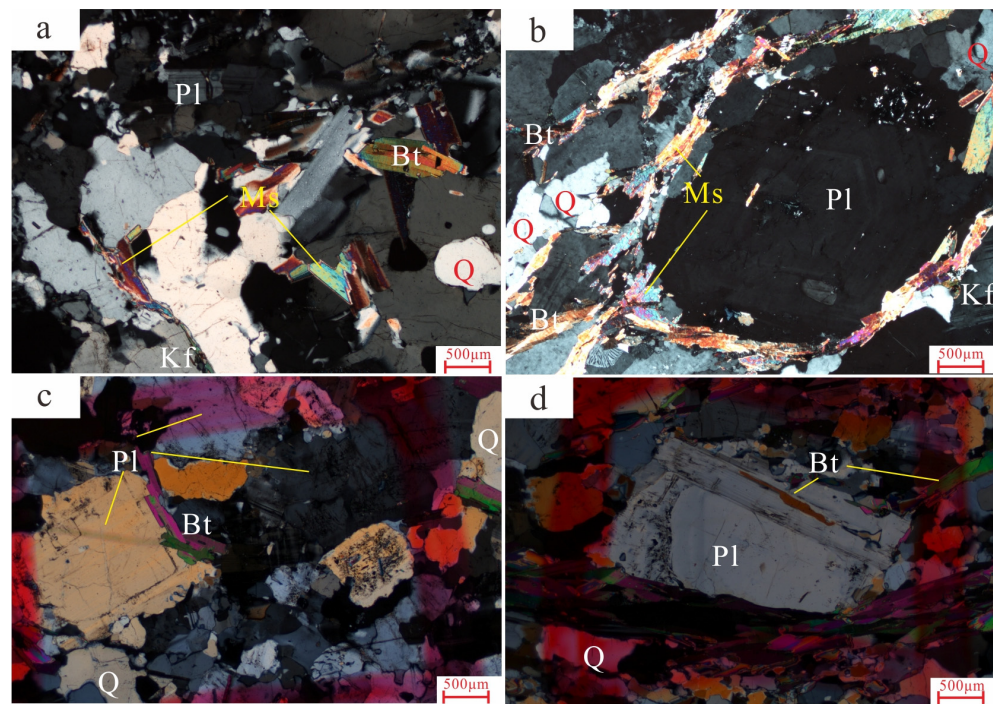


**Figure 3.** Representative photomicrographs of the Liemai muscovite granite. (a–d) are the microscopic photographs of plagioclase, K-feldspar, biotite, muscovite and quartz under orthogonal polarized light. (Bt—biotite; Ms—muscovite; Kf—K-feldspar; Pl—plagioclase; Q—quartz).

#### 4. Analytical Methods

##### 4.1. Zircon and Monazite U–Pb Geochronology Analysis

Laser ablation–inductively coupled plasma–mass spectrometry (LA-ICP-MS) U–Pb dating of zircon and monazite was performed at Wuhan Sample Solution Analytical Technology Co., Ltd., Wuhan, China. Please refer to Zong et al. (2010) [40] for detailed instrument parameters and analytical procedures. The spot size and frequency of the laser were set to 32  $\mu\text{m}$  and 8 Hz, respectively, in this study. Zircon 91500 and glass NIST 610 were used as external standards for U–Pb dating and trace element calibration, respectively. Each analysis incorporated a background acquisition of approximately 20–30 s followed by 50 s of data acquisition from the sample. The GeolasPro laser denudation system includes a COMPexPro 102 ArF 193-nm excimer laser and a MicroLas optical system with an ICP–MS instrument (Agilent 7700e). ICPMSDataCal software was adopted for offline data processing [41,42]. Isoplot/Ex\_ver3 [43] was used to obtain U–Pb age harmonic maps and calculate the age-weighted average of the zircon and monazite samples.

##### 4.2. In Situ Sr–Nd–Hf Isotope Analysis

In situ Sr isotope ratio analysis of feldspars, in situ Nd isotope ratio analysis of monazite, and in situ Hf isotope ratio analysis of zircon were conducted using a Neptune Plus multicollector (MC)-ICP-MS instrument (Thermo Fisher Scientific, Göttingen, Germany) in combination with a Geolas HD excimer ArF laser ablation system (Coherent, Göttingen, Germany) hosted at the Wuhan Sample Solution Analytical Technology Co., Ltd., Wuhan, China. For single-laser-spot ablation, the spot diameter ranged from 60 to 160  $\mu\text{m}$ , depending on Sr signal intensity. The pulse frequency was from 8 to 15 Hz, but the laser fluence was kept constant at  $\sim 10 \text{ J}/\text{cm}^2$ . The spot diameter ranged from 32 to 90  $\mu\text{m}$ , depending on Nd signal intensity. The pulse frequency was from 4 to 10 Hz, but the laser fluence was kept constant at  $\sim 8 \text{ J}/\text{cm}^2$ . Hf isotopes were acquired on zircon in single-spot ablation mode at a spot size of 44  $\mu\text{m}$ . Detailed instrument operating conditions and analytical methods can be found in Hu et al. (2015) [44]. Sr isotopic instrument mass fractionation correction was performed using the index rule, and the correction factor was estimated as

$^{88}\text{Sr}/^{86}\text{Sr} = 8.375209$  [45,46].  $^{143}\text{Nd}/^{144}\text{Nd}$  isotope instrument mass fractionation calibration was performed using the exponential rule. Please refer to the detailed description of the analytical method calibration process in Xu et al. (2015) [47].

#### 4.3. Whole-Rock Pb Isotope Analysis

Whole-rock Pb isotope analysis was performed at Wuhan Sample Solution Analytical Technology Co., Ltd., Wuhan, China. Pb isotope analysis was performed using a Thermo Fisher Scientific MC-ICP-MS instrument (Neptune Plus). A jet + X cone combination and dry pump were used during MC-ICP-MS analysis to improve the instrument sensitivity. The Pb international standard solution NBS SRM 981 (100  $\mu\text{g}/\text{L}$ ) was used as a quality control and external correction standard sample, and the  $^{208}\text{Pb}$  signal was generally higher than 6 V. Pb isotope instrument mass fractionation was corrected by the pseudo-internal standard index rule [48].

#### 4.4. Whole-Rock Major and Trace Element Analysis

Whole-rock major and trace element analyses were performed at the Wuhan Sample Solution Analytical Technology Co., Ltd., Wuhan, China. The major and trace elements were analyzed using a Primus II X-ray fluorescence spectrometry (XRF) instrument and Agilent 7700e ICP-MS instrument, respectively. To determine the main elements, the sample was ground into 200 mesh particles and dried. The total amounts of 6.0 g flux ( $\text{Li}_2\text{B}_4\text{O}_7$ :  $\text{LiBO}_2$ :  $\text{LiF} = 9:2:1$ ), 0.6 g sample, and 0.3 g oxidant ( $\text{NH}_4\text{NO}_3$ ) were weighed. To analyze the trace elements, the sample was ground into 200 mesh particles and dried, and 1 mL of high-purity  $\text{HNO}_3$  and 1 mL of high-purity HF were slowly added in sequence to a 50 g Teflon sample dissolving cartridge. Subsequently, the sample was first heated and then cooled, and a second drying process was conducted. The detailed process is described by Gao (2003) [49].

### 5. Analytical Results

#### 5.1. Zircon U–Pb Ages and Hf Isotopes

In this paper, the LA-ICP-MS zircon U–Pb test was performed targeting the edge of the Cenozoic zircon and the core of the inherited zircon. The test data are listed in Supplementary Table S2. There were 10 test points of zircon data at the edge. Of these, the U–Pb ages at points 01, 02, 24, and 37 were inconsistent due to the influence of residual zircon, which is not involved in the calculation of mixed ages. The U and Th contents in the remaining six new zircons were high, and the  $^{206}\text{Pb}/^{238}\text{U}$  age of the zircons varied between 41.1 and 42.9 Ma (Figure 4a,e, Supplementary Table S2). The weighted average age was  $42.1 \pm 0.76$  Ma (mean squared weighted deviations (MSWD) = 1.2), which represents the crystallization age of Liemai muscovite granite. This result is supported by the monazite U–Pb geochronology (Figure 5). In the selection of inherited zircon ages, we used the  $^{206}\text{Pb}/^{238}\text{U}$  age to calculate zircon ages less than 1000 Ma and employed the  $^{207}\text{Pb}/^{206}\text{Pb}$  age to calculate zircon ages greater than 1000 Ma. The inherited zircon core ages ranged from 258 to 2957 Ma (Supplementary Table S2). The  $^{206}\text{Pb}/^{238}\text{U}$  age at zircon measuring points No. 04, 07, 09, 12, 29, and 31 varied between 926 and 983 Ma, and the weighted average age was  $956 \pm 14$  Ma (MSWD = 2) (Figure 4b,c), indicating that the source rocks of the granite contained late Neoproterozoic–early Mesoproterozoic ancient zircons. The  $^{206}\text{Pb}/^{238}\text{U}$  ages at the No. 15, 16, and 20 zircon measuring points were relatively concentrated at 568 Ma in the concordant line, and the age-weighted average was  $559 \pm 58$  Ma (MSWD = 1.8) (Figure 4d), indicating that the source rock of the granite contained late Cambrian–Neoproterozoic ancient zircons. The oldest age of the inherited zircons was observed at measuring point No. 24, and the  $^{206}\text{Pb}/^{207}\text{Pb}$  age was 2954 Ma, indicating the Mesoarchean. The remaining core inherited zircon ages varied greatly, reflecting the diversity of the inherited zircon sources.

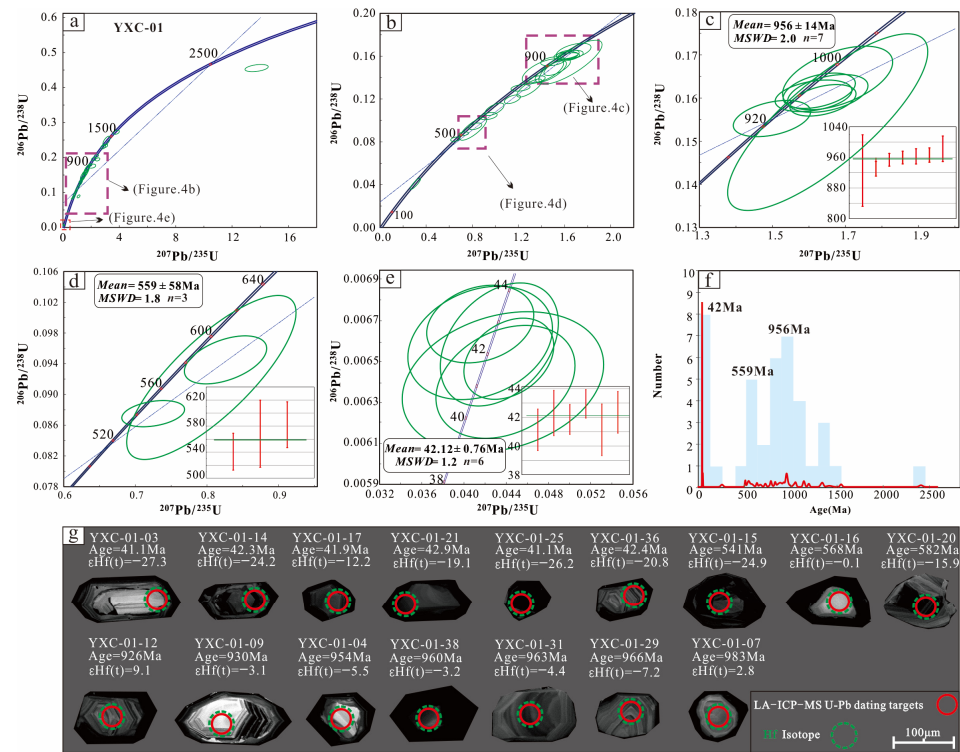


**Figure 4.** Concordia diagrams of zircon U–Pb ages and zircon CL images for the Liemai muscovite granites. The red solid circles show the spots of the LA-ICP-MS analyses for U–Pb zircon age; green dashed circles show the spots for the Hf isotopic analyses. (a) YXC-01 zircon age concordia diagram; (b–d) concordia diagram for inherited zircon cores; (e) concordia diagram for zircon rims; (f) age distribution curves and age distribution histogram of newborn and inherited zircons; (g) zircon cathodeluminescence diagrams of representative zircons.

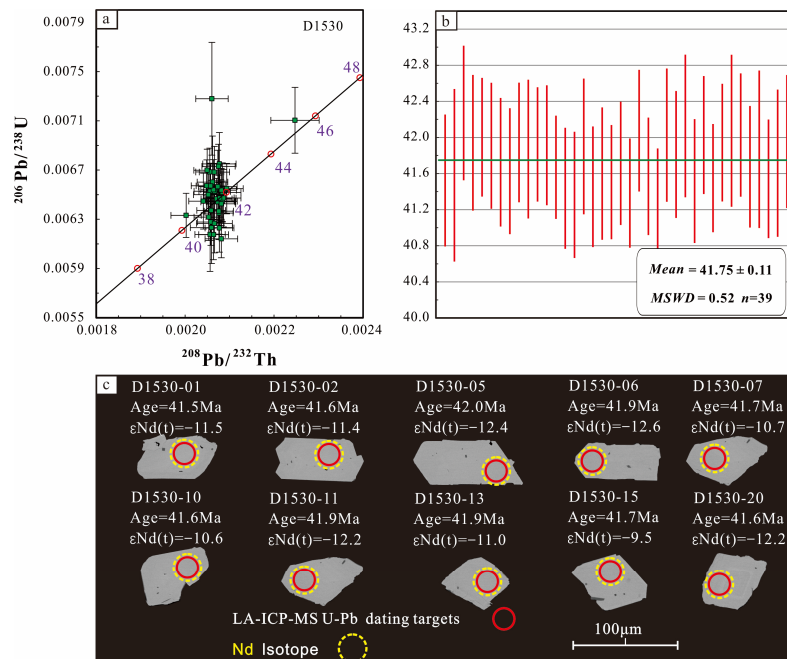


**Figure 5.** U-(Th)-Pb concordia diagram of monazites and CL images of representative monazites with corresponding  $^{208}\text{Pb}/^{232}\text{Th}$  ages. (a) D1530 monazite age concordia diagram; (b) the weighted mean age for monazites of the Liemai muscovite-granite; (c) monazite cathodeluminescence diagrams of representative monazites.

In this paper, the zircons in the YXC-01 sample of Liemai muscovite granite (data are provided in Supplementary Table S3) were subjected to LA–MC–ICP–MS Lu–Hf in situ isotope analysis. The  $^{176}\text{Hf}/^{177}\text{Hf}$  ratio of six magmatic zircons was in the range 0.281976–0.282403.  $\epsilon\text{Hf}(t)$  ranged from  $-12.2$  to  $-27.3$ , with an average value of  $-21.6$ . The two-stage depleted mantle model age ( $\text{TDM}_2$ ) varied between 1884 and 2831 Ma.

### 5.2. Monazite U–Pb Ages and Nd Isotopes

The monazite U–Th–Pb isotope and trace and rare earth element content analysis results for Liemai muscovite granite (D1530) are listed in Supplementary Tables S4 and S5, respectively. A backscattered image and the U–(Th)–Pb age of monazite are shown in Figure 5. Monazite in Liemai muscovite granite contains a high content of light rare earth elements (LREEs) and a low total amount of heavy rare earth elements (HREEs) (Supplementary Table S5). The  $^{207}\text{Pb}/^{235}\text{U}$  ages of monazite in Liemai muscovite granite are relatively dispersed, ranging from 55.4 to 224 Ma. Except for one monazite site not occurring on the concordia curve, the remaining  $^{206}\text{Pb}/^{238}\text{U}$  and  $^{208}\text{Pb}/^{232}\text{Th}$  ages are relatively concentrated. The  $^{206}\text{Pb}/^{238}\text{U}$  ages range from 39.5 to 46.8 Ma, and the  $^{208}\text{Pb}/^{232}\text{Th}$  ages range from 40.4 to 45.4 Ma. These ages are relatively concordant (Figure 5a). The weighted mean age is  $41.7 \pm 0.11$  Ma (MSWD = 0.52,  $n = 39$ ) (Figure 5b).

In this paper, samples of Liemai muscovite granite (D1530) were analyzed using in situ Nd isotope analysis. The detailed test data are listed in Supplementary Table S7. The ratio of  $\epsilon\text{Nd}(t)$  at the time of magma crystallization was calculated according to the data results. The in situ Nd isotope for monazite showed that the Nd isotope composition is low and stable. The initial value of  $^{143}\text{Nd}/^{144}\text{Nd}$  ranges from 0.511883–0.512038, and the  $\epsilon\text{Nd}(t)$  value ranges from approximately  $-12.56$  to  $-9.53$ .

### 5.3. In Situ Plagioclase Sr Isotopes

The Sr isotope data obtained for plagioclase are listed in Supplementary Table S8, and the beam positions are shown in Figure 6a,c. Because some plagioclase was pierced during the test, the black point data error was large, and the corresponding data did not participate in the calculation. The Sr isotope content in the plagioclase of the two Liemai muscovite granite samples is stable, indicating that the samples are not affected by assimilation and contamination. The plagioclase ( $^{87}\text{Sr}/^{86}\text{Sr}$ ) value of YXC-03 ranges from 0.724095 to 0.724717, with an average of 0.724498. The ( $^{87}\text{Sr}/^{86}\text{Sr}$ ) value of YXC-04 ranges from 0.720552 to 0.724491, with an average of 0.723456. The  $^{87}\text{Sr}/^{86}\text{Sr}$  ratios occur within the range of whole-rock Eocene adakitic rocks (Figure 6b,d), and the whole-rock Sr isotope results are provided in Supplementary Table S13.

### 5.4. Whole-Rock Pb Isotopes

The whole-rock Pb isotope composition of Liemai muscovite granite is summarized in Supplementary Table S9. The values of  $(^{206}\text{Pb}/^{204}\text{Pb})_i$ ,  $(^{207}\text{Pb}/^{204}\text{Pb})_i$ , and  $(^{208}\text{Pb}/^{204}\text{Pb})_i$  are 18.751–18.832, 15.708–15.735 and 39.197–39.379, respectively. All initial values are calculated using an age of 43 Ma. The whole-rock Pb isotope data are listed in Supplementary Table S13.

### 5.5. Whole-Rock Major and Trace Element Geochemistry

The whole-rock major and trace element results of five fresh Liemai muscovite granite samples are provided in Supplementary Table S6, and the major and trace element results for the Himalayan Eocene magmatic rocks (adakitic rocks and leucogranites) are listed in Supplementary Tables S10 and S11.

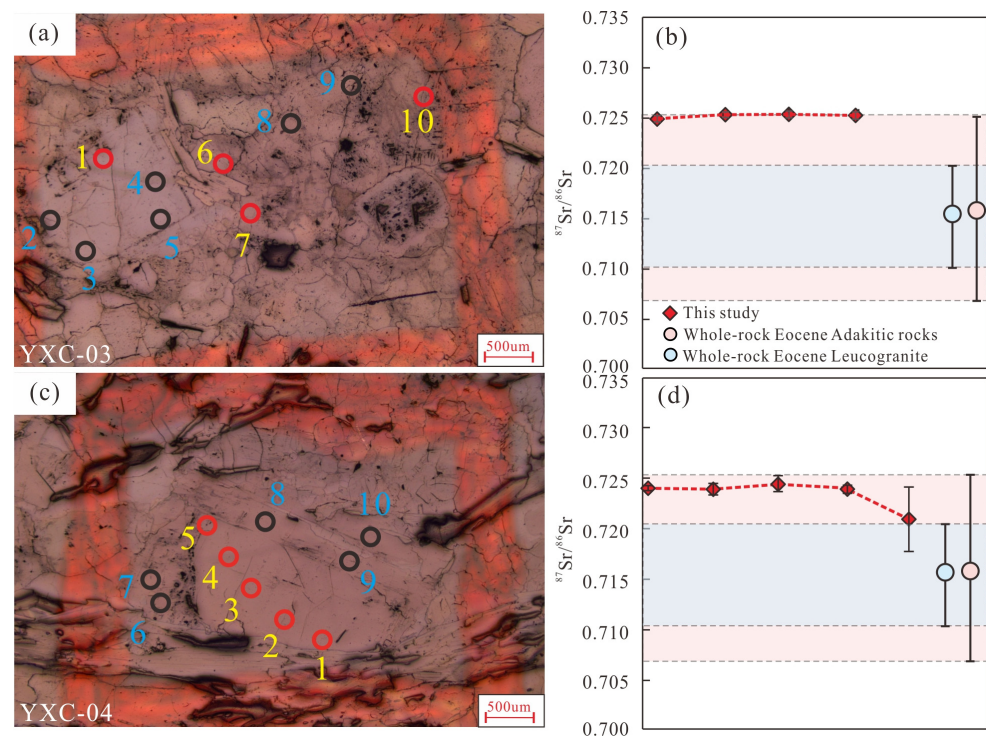


**Figure 6.** (a,c) Sr isotope point of LA-ICP-MS feldspar of Liemai muscovite granite. Comparison of whole-rock Sr isotope data between Eocene adakitic rocks and leucogranite (b,d). (Data from Supplementary Tables S10 and S11).

### 5.5.1. Adakitic Rock

Based on previous studies, geochemical analysis of 121 Himalayan Eocene adakitic rocks was conducted in this paper. The Himalayan Eocene adakitic rocks contained  $\text{SiO}_2$  (62.1–74.8 wt.%), with an average content of 70.1 wt.%, which is much higher than the total crustal content (60.6 wt.%). Moreover,  $\text{K}_2\text{O}$  (0.72–10.5 wt.%) was observed, with an average content of 3.24 wt.%, as well as  $\text{Na}_2\text{O}$  (1.82–5.81 wt.%), with an average content of 3.87 wt.%. The  $\text{K}_2\text{O}$  and  $\text{Na}_2\text{O}$  contents are higher than those in the total crust (1.81 and 3.07 wt.%, respectively), and  $\text{Na}_2\text{O}/\text{K}_2\text{O} > 1$ . The average content of  $\text{CaO}$  is 2.34 wt.%. The average  $\text{Al}_2\text{O}_3$  content is 18.95 wt.%, the average A/NK value is 1.62, and the average A/CNK value is 1.13. The  $\text{P}_2\text{O}_5$  content is 0.03–0.31 wt.%. The  $\text{MgO}$  content is low, between 0.04 and 2.08 wt.%, with an average value of 1.0 wt.%, which is much lower than the total crustal content (4.66 wt.%). The results show that the Himalayan Eocene adakitic rocks are high-K calc-alkaline peraluminous granites (Figure 7c,d). In this paper, considering five fresh Liemai muscovite granite samples, the  $\text{SiO}_2$  content is 68.3–75.5 wt.%, the  $\text{Al}_2\text{O}_3$  content is 15.1–16.1 wt.%, and the total alkali  $\text{Na}_2\text{O} + \text{K}_2\text{O}$  content is 5.26–8.43 wt.%. Moreover, the  $\text{MgO}$  content is 0.14–0.98 wt.%, the A/NK value is 1.32–2.02, and the A/CNK value is 1.1–1.15. In the petrological Q–A–P classification diagram (Figure 7a), the five samples are plotted in the monzonitic granite area, except for one sample that is plotted in the granodiorite area. The  $\text{Na}_2\text{O} + \text{K}_2\text{O}/\text{SiO}_2$  petrological classification diagram (Figure 7b) shows that the adakitic rocks are plotted in the granite or granodiorite area.

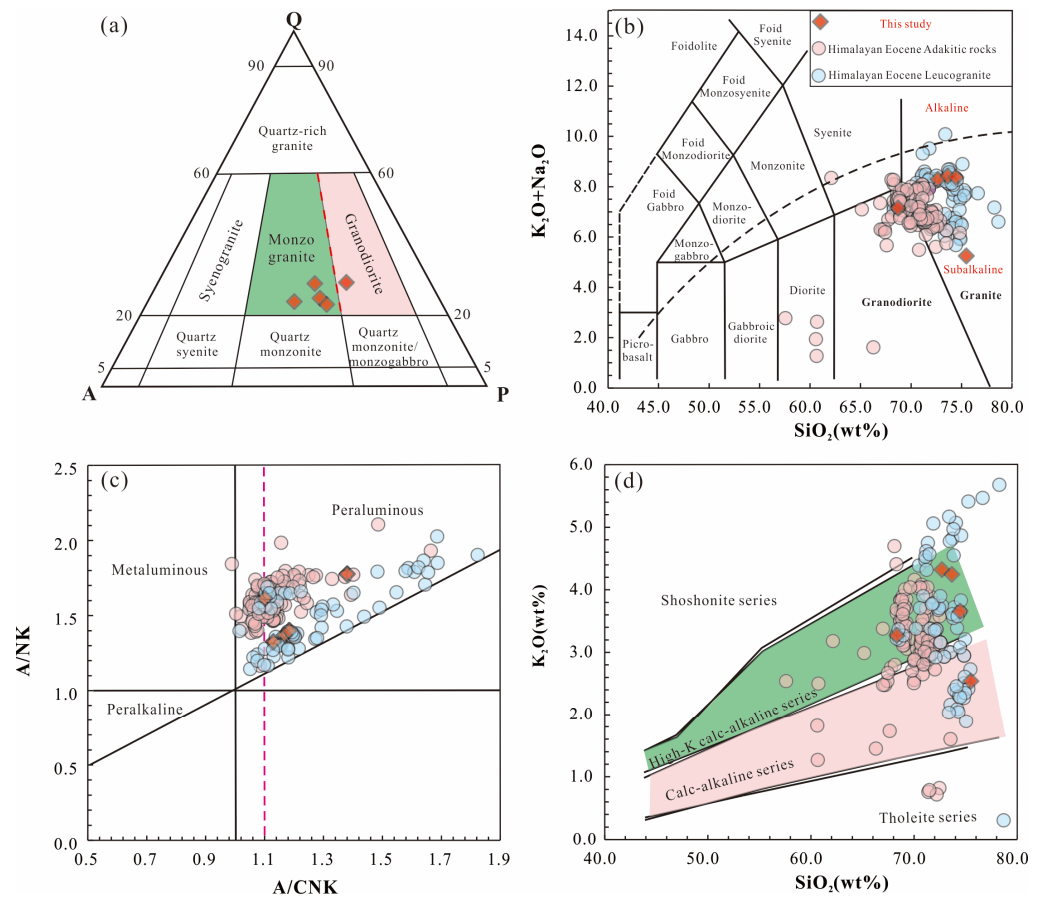


**Figure 7.** (a) Q-A-P lithology discriminant diagram of the Leimai granites (after Middlemost, 1994) [50]; (b) plots of  $\text{SiO}_2$  versus  $\text{Na}_2\text{O} + \text{K}_2\text{O}$  (according to Middlemost, 1994) [50]; (c)  $\text{Al}_2\text{O}_3 / (\text{CaO} + \text{Na}_2\text{O} + \text{K}_2\text{O})$  versus  $\text{Al}_2\text{O}_3 / (\text{Na}_2\text{O} + \text{K}_2\text{O})$  diagram (according to Maniar and Piccoli, 1989) [51]; (d)  $\text{SiO}_2$  versus  $\text{K}_2\text{O}$  diagram (after Peccerillo and Taylor, 1976) [52].

The primitive mantle-normalized trace element distribution diagram shows that the Liemai muscovite granite yields a distribution curve similar to that of adakitic rocks (Figure 8a,c). The characteristics of adakitic rocks include relative enrichment of large-ion lithophile elements (LILEs) such as Rb; moreover, high-field-strength elements (HFSEs) such as U and Pb are relatively enriched, Nb, Ta and Zr are relatively depleted, and the Sr elemental content is high, with an average value of  $354.2 \times 10^{-6}$ . Eocene adakitic rocks are enriched in LREEs ( $119.3 \times 10^{-6}$ ) and depleted in HREEs ( $6.9 \times 10^{-6}$ ), with weak or no Eu anomalies. The LREE/HREE ratio varies between 10 and 20, with an average of 17.8, indicating a clear right-leaning model (Figure 8d). The average LREE [(La/Yb)<sub>N</sub>] value is 40.2, indicating that the internal fractionation of LREEs is relatively high. The content of Ho-Lu elements in the rare earth element distribution model decreases or stabilizes in turn [53].

### 5.5.2. Leucogranite

The geochemical analysis of 68 Himalayan Eocene leucogranite samples is described in this paper. The values of the major elements of Eocene leucogranite do not differ from the mean values of total crustal major elements. Leucogranite exhibits the following characteristics: (1) high silicon ( $\text{SiO}_2$ ) content (68.3–73.8 wt.%), with an average of 73.1 wt.%, which is much higher than the total crustal content (60.6 wt.%); (2) high alkalinity, including  $\text{K}_2\text{O}$  (0.3–6.7 wt.%), with an average of 3.59 wt.%, and  $\text{Na}_2\text{O}$  (1.5–6.3 wt.%), with an average of 4.01 wt.%, both of which are higher than the total crustal  $\text{K}_2\text{O}$  and  $\text{Na}_2\text{O}$  contents (1.81 and 3.07 wt.%, respectively), with  $\text{Na}_2\text{O}/\text{K}_2\text{O} > 1$ ; (3) relatively low CaO content, with

an average of 1.02 wt.%; (4) high  $\text{Al}_2\text{O}_3$  content, with an average value of 14.97 wt.%, the average A/NK value is 1.49, and the average A/CNK value is 1.27; and (5) low  $\text{MgO}$  content, between 0.02 and 1.47 wt.%, with an average of 0.35 wt.%, which is much lower than the total crustal content (4.66 wt.%). In summary, the Eocene leucogranite is a high-K calc-alkaline peraluminous granite (Figure 7c,d). In the trace element distribution diagram (Figure 8e), the leucogranite is characterized by enriched LILEs (such as Rb) and U, Ta, and Pb elements, depleted HFSEs (such as Nb and Zr) and La and Nd elements, with obvious negative Sr, Ba and Eu anomalies. The content of REEs in the light granite exhibits a narrow range ( $\Sigma\text{REE} = 9.4 \times 10^{-6}$ – $182.2 \times 10^{-6}$ ), with an average value of  $68.9 \times 10^{-6}$ , which is lower than the average value of the total crust ( $106.2 \times 10^{-6}$ ). The LREE/HREE ratio mainly varies between 2.6 and 22.4, with an average value of 10.7. In addition to the obvious negative Eu anomaly in leucogranite, the normalized rare earth model distribution curve of the other chondrites is relatively flat (Figure 8f).

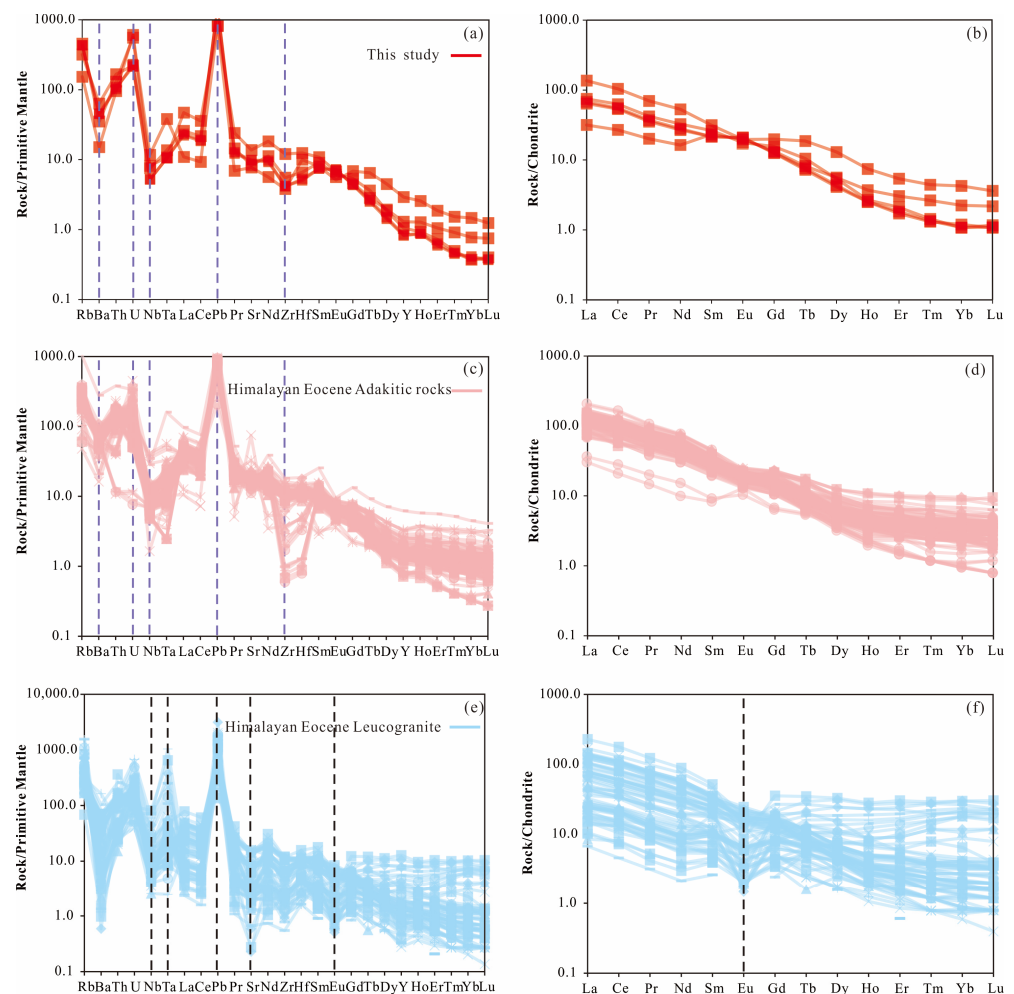


**Figure 8.** Rare earth element chondrite-normalized diagrams and primitive mantle-normalized trace element diagrams of the Leimai two-mica granite and other granitoids in the study area. (a,c,e) Standardized map of REE chondrites; (b,d,f) standardized map of trace element primitive mantle.

## 6. Discussion: Relationship between Adakitic Rocks and Leucogranite

### 6.1. Chronological Characteristics

In this paper, the in situ U–Pb ages of U-bearing accessory minerals such as zircon, monazite, and titanite in Himalayan Eocene magmatic rocks are statistically analyzed (Supplementary Table S12), and the age distribution of the analyzed Himalayan Eocene magmatic rocks is shown in Figure 9. We note that Eocene magmatic rocks are found only

in the northern Himalayas and are dominated by leucogranite and adakitic rocks. Figure 9a shows that the Himalayan Eocene magmatic rocks mainly developed in two time stages, early Eocene (51–40 Ma) and late Eocene (39–34 Ma), and the age distribution exhibits three peaks: 47–43 Ma, 42–40 Ma and 37–35 Ma. To explore the significance of the study for the chronology of Eocene granite, we determined the age of the exposed rock mass in the northern Himalayas.

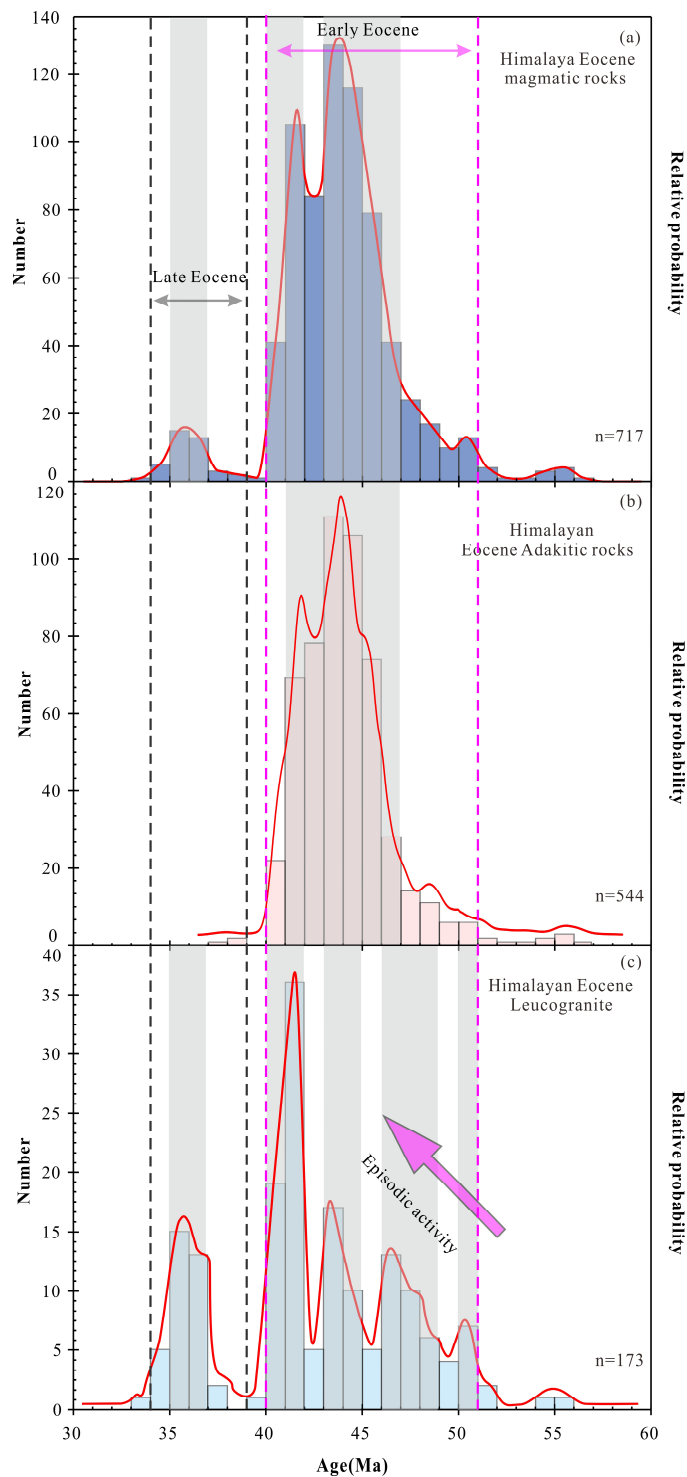


**Figure 9.** U-(Th)-Pb age distribution of Himalayan Eocene magmatic secondary minerals (Zircon/Monazite/Titanite). (a) Age distribution of Himalayan Eocene magmatic rocks; (b) Age distribution of Himalayan Eocene adakitic rocks; (c) Age distribution of Himalayan Eocene leucogranites.

Early Eocene (51–40 Ma) magmatic rocks are preserved only in the northern Himalayan belt, with a peak at 44 Ma [24]. The Eocene leucogranites are mainly exposed in the Lhagoi Kangri dome [26], the Ramba dome [54] and the Yalaxiangbo dome [11]. The magmatic rocks of Rongbo in Langkazi County and Dala, Quedang, and Liemai in Longzi County are dominated by adakitic two-mica granites with mafic enclaves [10,21–25,31,54–56]. Hawen in Langkazi County, Langshan in Gyangze County and Zhegucuo in Cuomei County contain intermediate-mafic granodiorite, gabbro and high-Mg diorite, respectively [57–59]. Late Eocene (39–31 Ma) magmatic rocks are less exposed and are most developed in the gneiss domes of the northern Himalaya, with a peak at 35 Ma, including the Yalaxiangbo dome [30], Changguo dome [60], Xiaru dome [61], Lhagoi Kangri dome [26] and Cuonadong dome [62]. The lithology is dominated by leucogranite.

The data show that the ages of 544 Eocene adakitic rock samples mainly range from 47 to 41 Ma and from 43 to 42 Ma (Figure 9b). The ages of 173 leucogranite samples show a continuous distribution with five peaks (Figure 9c), at 51–50 Ma, 49–46 Ma, 45–43 Ma, 42–40 Ma and 37–35 Ma. In summary, we found that leucogranites were actively generated throughout the Eocene, and a clear episodic growth trend occurred from 51 to 40 Ma. Adakitic rocks only significantly developed during the early Eocene (47–40 Ma), and the development of adakitic rocks was inhibited from 40 to 35 Ma, which may represent a tectonic transition period. The leucogranites formed from 40 to 37 Ma also indicated a low age peak, suggesting that they may have been affected by the same tectonic events as adakitic rocks.

## 6.2. Petrogenesis

As mentioned above, adakitic rocks and leucogranites exhibit different characteristics of their major and trace elements (Figures 7 and 8, respectively). Similarly, through the study of chronology, we found that the peak values of these two rocks differed significantly, at 51–40 Ma and 40–35 Ma, respectively, indicating that the two must have experienced differences in rock genesis. Based on the characteristics of the major and trace elements and the  $Y$ - $Sr/Y$  and  $Yb_N$ - $La_N/Yb_N$  ratios (Figure 10), Liemai muscovite granite is similar to adakitic rock.

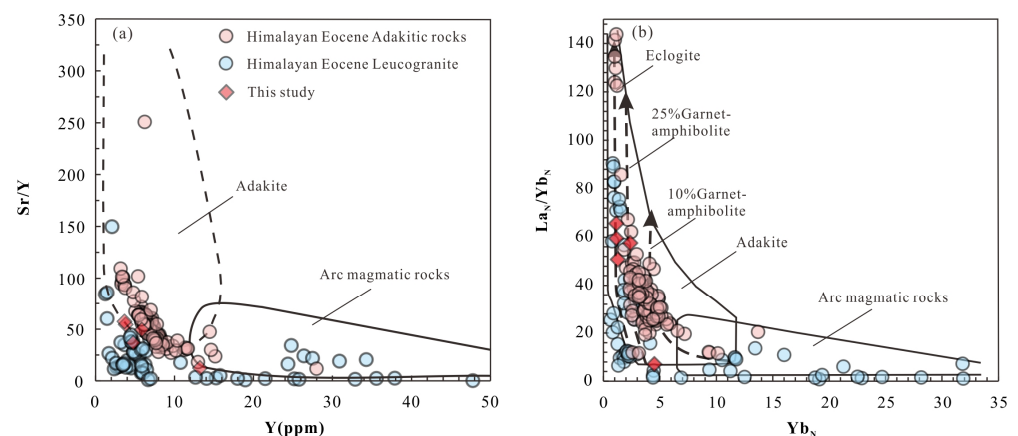


**Figure 10.** Geochemical discrimination diagrams of (a)  $Y$  versus  $Sr/Y$  and (b)  $Yb_N$  versus  $La_N/Yb_N$  (Defant and Drummond, 1990) [63].

The Sr-Nd isotopes show that the Eocene adakitic rocks and leucogranites exhibit similar source characteristics, and their source is likely the Greater Himalayan complex dominated by garnet amphibolite (Figure 11a). This view is supported by Zeng et al. (2011) [10], who proposed that the Eocene granite source rock in the Yalaxiangbo dome is dominated by amphibolite. The main minerals (such as feldspar and mica) in granite can control the geochemical behavior of elements such as Sr and Ba. A large amount of plagioclase remains in the melting process of sandstone, while a small amount of plagioclase remains in the melting process of pelite [64–66]. Therefore, the  $Rb/Sr$  and  $Rb/Ba$  ratios of

a sandstone-derived melt are significantly higher than those of a pelite-derived melt [67]. As shown in the Rb/Sr-Rb/Ba diagram (Figure 11b), the Eocene adakite source rocks are mainly argillaceous rocks with less clay, little plagioclase and some basic components. The leucogranite is mainly a clay-rich, multiplagioclase pelite, which contains sandstone components. Sylvester (1998) [67] proposed that the lower CaO/Na<sub>2</sub>O ratio of strongly peraluminous granites generally indicates that the granite source area involves pelite melting, while a higher CaO/Na<sub>2</sub>O ratio indicates a psammite melting source area. The ratio of the major elements of Eocene adakitic rocks and leucogranites conforms to this feature (the CaO/Na<sub>2</sub>O ratio of the two is 0.91 > 0.26; Supplementary Tables S10 and S11).

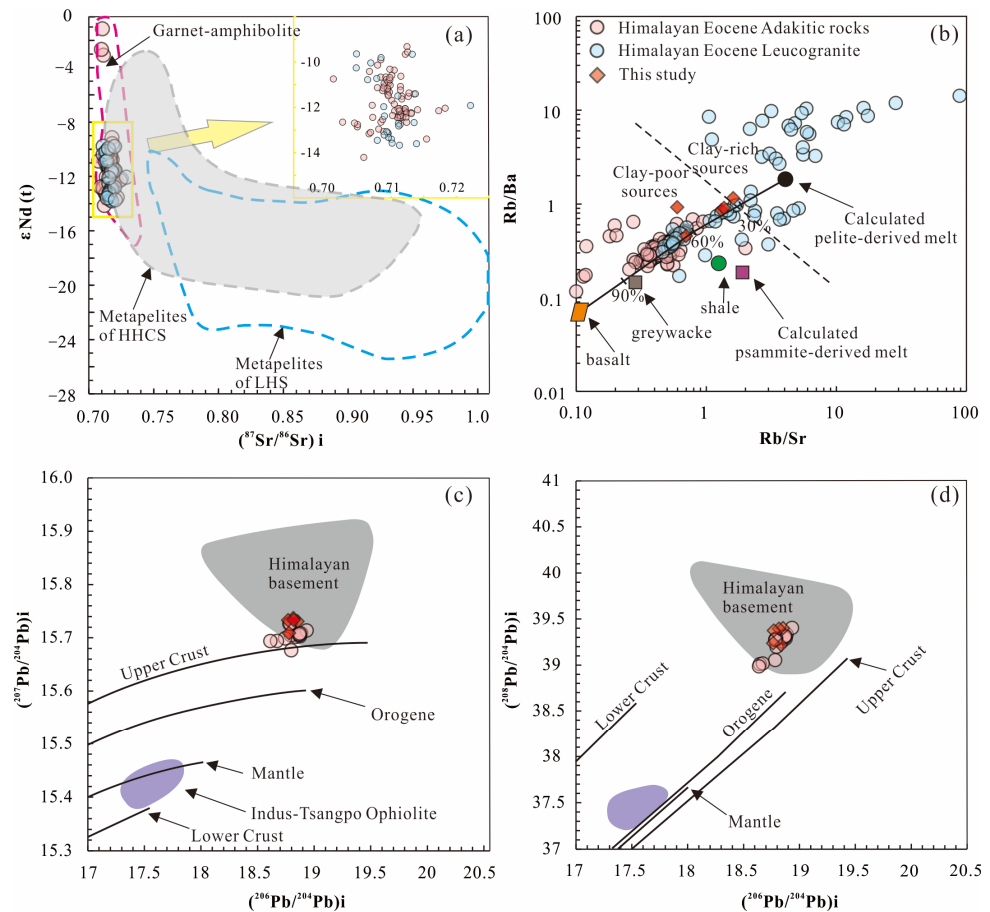


**Figure 11.** Diagrams of (a)  $\epsilon\text{Nd}(t)$  versus  $^{87}\text{Sr}/^{86}\text{Sr}(i)$ ; (b) Rb/Ba versus Rb/Sr (after Sylvester, 1998) [67]; (c)  $^{206}\text{Pb}/^{204}\text{Pb}$  versus  $^{207}\text{Pb}/^{204}\text{Pb}$  and (d)  $(^{206}\text{Pb}/^{204}\text{Pb})_i$  versus  $(^{208}\text{Pb}/^{204}\text{Pb})_i$  for the Liemai muscovite granites.

Due to the lack of Pb isotope records for Eocene leucogranite, only whole-rock Pb isotopes of adakitic rocks were analyzed in this paper, and it was determined that the Pb isotope composition of Eocene adakitic rocks is similar to that of the Himalayan basement (Figure 11c,d). In the  $\epsilon\text{Hf}(t)$  and U–Pb age maps, all the sample sites were plotted below the chondrite evolution line, indicating that Eocene adakitic rocks and leucogranites were derived from the ancient crust (Figure 12).

In this paper, the saturation temperature of Eocene adakitic rock and leucogranite was measured based on whole-rock Zr and whole-rock rare earth elements. The results show that the average whole-rock Zr-based temperature ( $T_{\text{Zr}}$ ) of adakitic rock is 699.2 °C, and the average whole-rock rare earth element-based temperature ( $T_{\text{LREE}}$ ) is 827.2 °C. The average whole-rock Zr-based temperature ( $T_{\text{Zr}}$ ) of leucogranite is 636.6 °C, and the average whole-rock rare earth element-based temperature ( $T_{\text{LREE}}$ ) is 757.4 °C [53] (Figure 13a,b). Both crystallization temperatures indicate that the saturation temperature of adakitic rock

is approximately 60 °C higher than that of leucogranite. We have previously estimated the crystallization pressure of Eocene adakitic rocks and leucogranites [68,69]. The results revealed that the crystallization pressure of adakitic rocks is much higher than that of leucogranites. The average crystallization pressures of adakitic rocks and leucogranites are 2147 and 1312 MPa, respectively, showing a decreasing trend with age (Figure 13c).

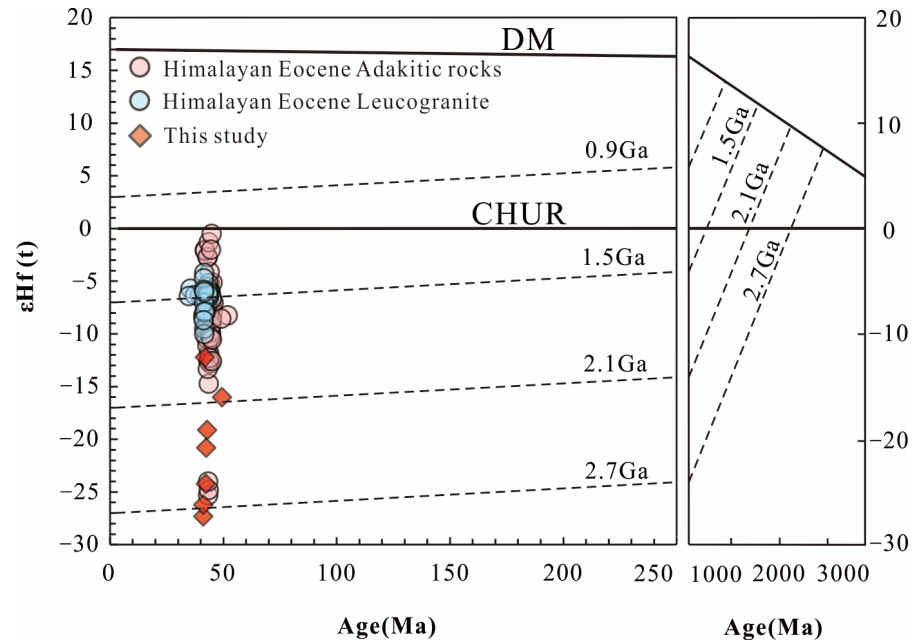


**Figure 12.** Plot of  $\epsilon\text{Hf}(t)$  versus zircon U–Pb ages for the Liemai muscovite granites. Data sources: see Supplementary Table S13.

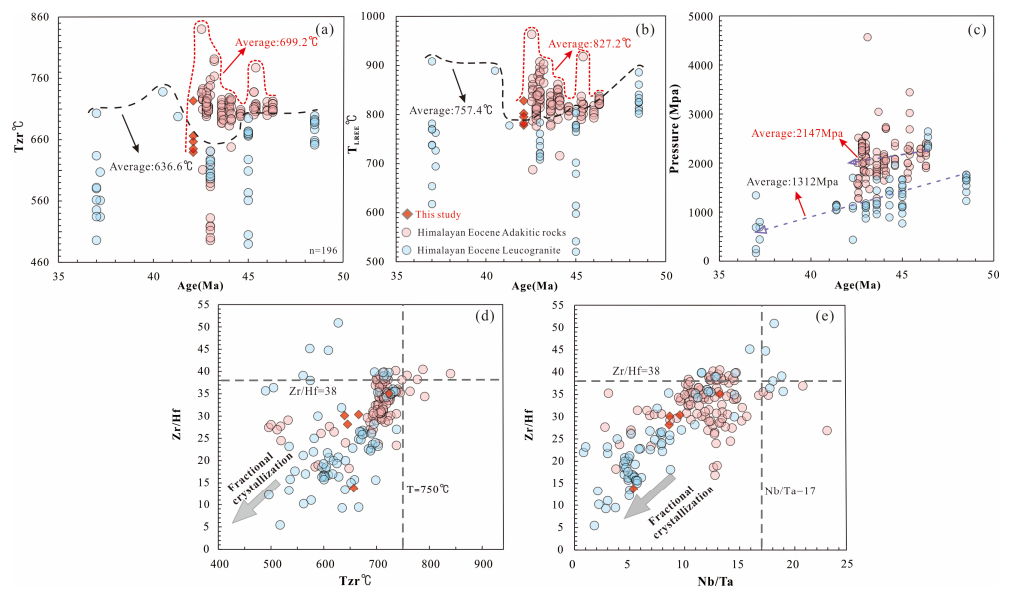


**Figure 13.** Age versus  $T_{\text{Zr}}$  °C (a) and TLREE °C (b) diagram of the Himalayan Eocene leucogranite and adakitic rocks, China. Data cited from Supplementary Tables S11–S13; (c) Diagrams of Pressure versus Age (Ma); (d) Diagrams of  $T_{\text{Zr}}$  °C versus Zr/Hf; (e) Identification diagram of the evolutionary types of Nb/Ta versus Zr/Hf granite (after Breiter and Škoda, 2017) [70].

The data in this paper show that the diagenetic pressure of the Eocene magma developed in the northern Himalayas exhibited a decompression trend from 45 to 37 Ma, and the magmatic activity was weak from 40 to 35 Ma, indicating that there was a short-term tectonic stress adjustment. This view is supported by those of Štípská et al. (2020) [71]

and Kawabata et al. (2021) [72] regarding retrograde metamorphism and decompressional partial melting, respectively. The Zr/Hf– $T_{Zr}$  temperature diagram and Zr/Hf–Nb/Ta diagram (Figure 13d,e, respectively) show that the degree of fractional crystallization of the Himalayan Eocene leucogranite is much higher than that of the adakitic rock. The Zr/Hf– $T_{Zr}$  temperature diagram and Zr/Hf–Nb/Ta diagram (Figure 13d,e, respectively) show that the degree of fractional crystallization of the Himalayan Eocene leucogranite is much higher than that of the adakitic rock.

Seven genetic models of adakitic rocks (YalaXiangbo dome, Ranba dome, Dala, Quedang, Liemai, etc.) exposed in the eastern Himalayas were examined one by one, including the following: ① The Sr, Nd and Hf isotope characteristics and geochemical differences all reflect the characteristics of granite crust sources. Before 65 Ma, the Himalayas were located at passive continental margins, and there was no subducted oceanic crust beneath. Therefore, the cause of partial melting of the subducted oceanic crust plate is excluded [22,73,74]; ② the crust source characteristics of granite and many ancient inherited zircons exclude the genesis of partial melting of the lower crust of underplating basaltic rocks [75]; ③ the MgO, Mg#, Cr and Ni contents in the granite are lower than those in the metasomatism products of the delaminated lower crust and mantle peridotite, which excludes the origin of partial melting of the delaminated lower crust [63,76,77]; ④ the main collision stage of the India–Eurasia continent encompasses crustal shortening, pressurization and warming, which excludes the cause of water-induced partial melting of high-grade metamorphic rocks under abnormal heat due to rapid exhumation [78]; ⑤ there exists no correlation between  $\epsilon Nd(t)$  and  $^{147}Sm/^{144}Nd$  and  $SiO_2$  in granites, while very little mantle-derived magma is exposed in the eastern Himalayas, and the Langshan gabbro ( $45 \pm 1.1$  Ma) is 500 km away. Therefore, the possibility of magma mixing between felsic and basaltic magmas is excluded [58,79]; ⑥ Adakitic rocks indicate no trend of low-pressure fractional crystallization, which excludes the crustal assimilation and fractional crystallization process of basaltic magma. Finally, previous authors have determined that the adakitic rocks in the eastern part of the Himalayas are the product of partial melting of the basic materials of the thickened lower crust [80]. The eastern part of the Eocene Himalayas occurs at the Indian–Eurasian continental collision stage. The tectonic background is the continuous thickening of the crust, and the crust thickness is  $>50$  km. The Liemai muscovite granite considered in this paper exhibits geochemical characteristics similar to those of adakitic rocks in the adjacent area. Therefore, the Liemai granite is the product of partial melting of the thickened lower crust, which is supported by Dai et al. (2023) [21] and Tian et al. (2020) [31].

The above determination of the granite source area, magmatic crystallization temperature, crystallization pressure and tectonic background lay the foundation for the subsequent discussion in this paper. Therefore, it is proposed that the difference in the characteristics of the major and trace elements between Eocene adakitic rocks and leucogranites indicate that they may have undergone different magmatic processes [10,11,21–23]. The correlation between the main elements is shown in the Harker diagram (Figure 14a–l),  $Al_2O_3$ , MgO and CaO exhibit obvious linear decreasing trends because the separation and crystallization of plagioclase leads to decreases in certain main elements (Figure 14a,d,e) and there exists no obvious linear relationship between  $Na_2O$ ,  $K_2O$  and  $N_2O/K_2O$ , which may be affected by the end-member characteristics of granite crystallization differentiation [61] (Figure 14b,c,f). Usually, high-pressure fractional crystallization of basaltic melts (involving garnet) yields a unique geochemical trend. For example, the Sr/Y, Dy/Yb, Ba and  $(La/Yb)_N$  ratios and  $Al_2O_3$  content significantly increase with increasing  $SiO_2$  content [80]. Obviously, in Figures 13a and 14i–l, there is no obvious change trend in Eocene adakitic rocks, and leucogranite exhibits an obvious linear trend of low-pressure fractional crystallization, indicating that the leucogranite is significantly affected by fractional crystallization of plagioclase. This result is consistent with the genesis of low-magnesian granite determined by Zeng et al. (2014) [11] and Dai et al. (2023) [21]. The magmatic crystallization differentia-

tion attributed to fractional crystallization of plagioclase may be reflected in the melt of peraluminous leucogranite.

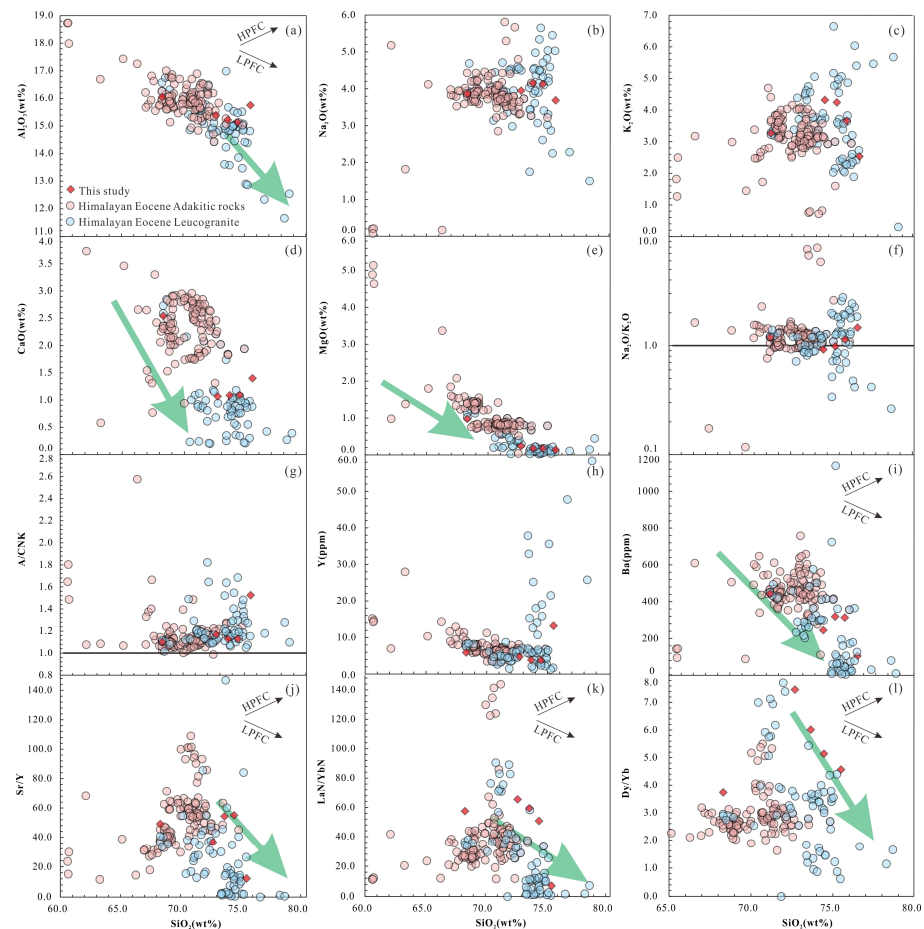


**Figure 14.** Diagrams of major element and trace element ratios versus  $\text{SiO}_2$  in Eocene magmatic rocks of the Himalayas. (a)  $\text{Al}_2\text{O}_3$  versus  $\text{SiO}_2$  diagram; (b)  $\text{Na}_2\text{O}$  versus  $\text{SiO}_2$  diagram; (c)  $\text{K}_2\text{O}$  versus  $\text{SiO}_2$  diagram; (d)  $\text{CaO}$  versus  $\text{SiO}_2$  diagram; (e)  $\text{MgO}$  versus  $\text{SiO}_2$  diagram; (f)  $\text{Na}_2\text{O}/\text{K}_2\text{O}$  versus  $\text{SiO}_2$  diagram; (g) A/CNK versus  $\text{SiO}_2$  diagram; (h) Y versus  $\text{SiO}_2$  diagram; (i) Ba versus  $\text{SiO}_2$  diagram; (j) Sr/Y versus  $\text{SiO}_2$  diagram; (k)  $(\text{La}/\text{Yb})_N$  versus  $\text{SiO}_2$  diagram; (l) Dy/Yb versus  $\text{SiO}_2$  diagram; The green arrows represent the trend of element content ratio changes with increasing magmatic acidity and differentiation. HPFC: high-pressure fractional crystallization involving garnet (Macpherson et al., 2006) [81]; LPFC: low-pressure fractional crystallization involving olivine + clinopyroxene + plagioclase + hornblende + titanomagnetite (Castillo et al., 1999) [82].

As an incompatible element, Th is not easily affected by rock weathering and alteration and can remain stable in separation crystallization and assimilation contamination processes [83]. Therefore, we use the incompatible element Th as an effective index to determine the genesis of rocks. The experimental data show that garnet remains stable under pressures higher than  $\sim 1.0$  GPa (a thickness of approximately 33 km), and amphibole remains stable at  $\leq 2.2$ – $2.5$  GPa [84]. The stability of plagioclase is closely related to the  $\text{H}_2\text{O}$  content, and it remains stable under pressures  $< 1.0$  GPa in the presence of aqueous fluid. However, in the case of dehydration melting, the stability pressure reaches as high as 1.5–1.8 GPa (a thickness of approximately 50–60 km) [85–87]. In deep crust environments ( $> \sim 1.0$  GPa), Y and Yb preferentially dissolve into garnet or amphibole in the process of fractional crystallization and crystallization differentiation of granite, while Sr and La enter the melt to form magmatic melt with high Sr/Y and La/Yb ratios. In shallow crustal environments ( $< \sim 1.0$  GPa), Sr preferentially enters plagioclase, Y and Yb enter the melt, and the Sr/Y and La/Yb ratios are low [13,88].

In the trace element Harker diagram, there is no linear correlation between Rb and Sr (Figure 15a,b), the trace element characteristics of leucogranite indicate an obvious linear relationship among Y, Yb, Ba, LREE (Figure 15c–f). During the evolution of Eocene adakitic rocks, Yb and Y are basically in a stable state, indicating that adakitic rocks with high Sr/Y ratios may occur in deep crust environments ( $>1.0$  GPa, average of 2.15 GPa), and amphibole and garnet remain in a stable state. In contrast, light-colored granite with a low Sr/Y ratio occurs in medium- to high-pressure environments ( $>1.0$  GPa, with an average of 1.31 GPa) in the deep crust, and a certain degree of amphibole dehydration partial melting likely occurs to maintain plagioclase stability, which is also consistent with the classification characteristics of granite under different pressures explained by Zhang et al. (2006) [89].

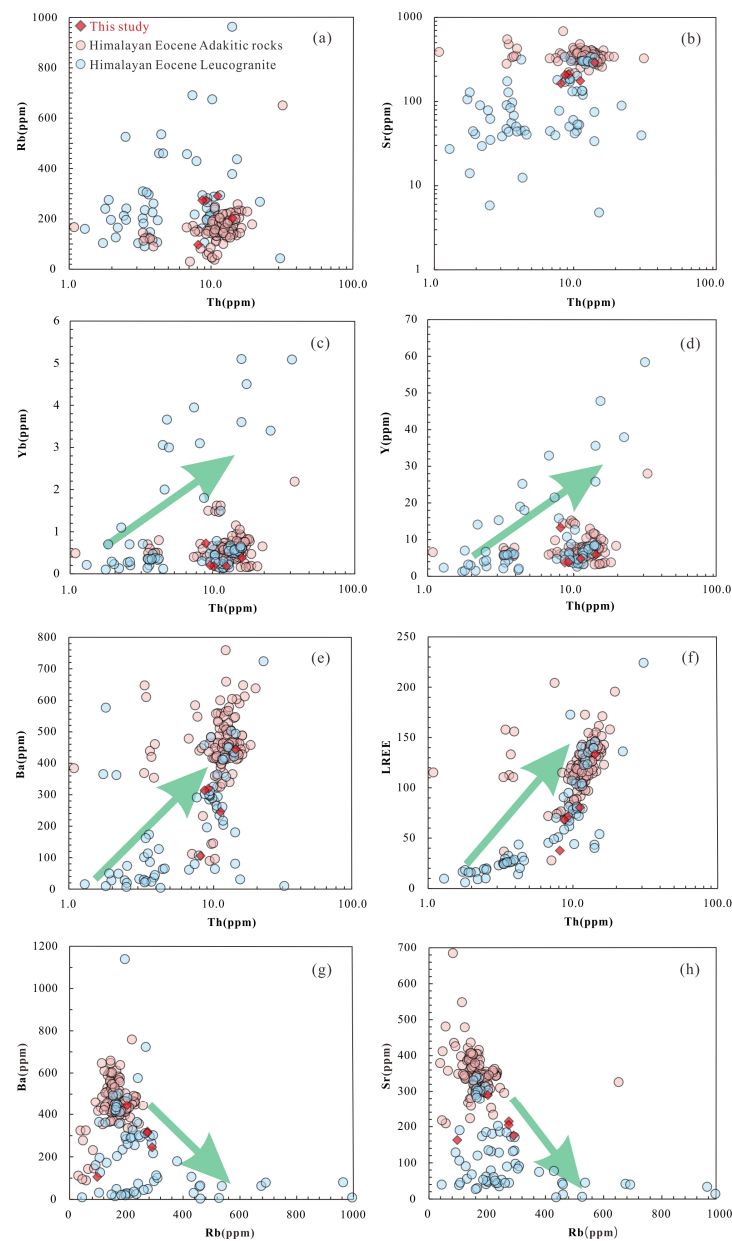


**Figure 15.** Variation diagrams for representative trace elements. (a) Rb versus Th diagram; (b) Sr versus Th diagram; (c) Yb versus Th diagram; (d) Y versus Th diagram; (e) Ba versus Th diagram; (f) LREE versus Th diagram; (g) Rb versus Ba diagram; (h) Rb versus Sr diagram; The green arrow represents linear correlation.

A previous paper revealed that adakitic rocks are strongly depleted in HREEs and that Ho to Lu exhibit slightly inclined or flat characteristics, reflecting the presence of garnet and amphibole in the residual phase during partial melting. The absence of Eu anomalies shows that the adakitic rocks have not experienced obvious separation and crystallization of plagioclase. Notably, plagioclase exists as a reaction phase during partial melting [90]. The fractional crystallization of plagioclase leads to decreases in the Ba and Sr contents in felsic magma (Figure 15g,h). The LREE and Th elements in Eocene leucogranite exhibit obvious depletion characteristics, indicating that a certain degree of monazite separation and crystallization has occurred [91,92].

In summary, we conclude that the genesis mechanisms of Liemai granite and Eocene adakitic rock are consistent, being a result of partial melting of metapelite dominated by amphibolite in the deep crust in a high-temperature and high-pressure environment in the crustal thickening process. Leucogranite is the result of the ascending emplacement migration process against the same geological background in a lower-temperature and lower-pressure environment and continuous fractional crystallization dominated by plagioclase. At the same time, this explains the episodic age distribution of leucogranite.

### 6.3. Tectonic Implications

Through the review of magmatic records of the early tectonic evolution of the Himalayan region and the division of tectonic stages by previous researchers, it has been proposed that it would be difficult for early prograde metamorphism to produce large-scale crustal anatexis [2,5,10,11,23]. Therefore, the development of Himalayan magmatism requires additional mechanisms, such as heating and decompression. In this study, we focused on the Himalayan Eocene (55–35 Ma).

During the early Eocene (50–45 Ma), the leading edge of the Indian continental crust subducted northward under the Lhasa plate. In contrast, the THS in the upper crust was thrust southward along the southern Tibetan thrust system, resulting in low-grade metamorphism and formation of the Himalayan fault–fold belt [93], and the whole Himalayan crust was shortened and thickened [94]. Previous scholars have found that although the metamorphic times of the eastern and western parts of the Himalayas are almost the same, at 47–45 Ma [84,95] and 47–46 Ma [96], respectively, the metamorphic facies in the two parts differ. The metamorphic facies in the eastern part of the Himalayas is a high-pressure amphibolite–granulite facies, while the facies in the western part is a high-ultrahigh pressure eclogite facies. This may be related to the angle of the subducting Indian continental crust plate [93]. Gentle subduction occurred in the eastern Himalayas at a low angle up to a depth of 20–30 km [2,93], while deep subduction occurred in the Indian continental crust at a high angle up to a mantle depth of 90–100 km in the western Himalayas. During the middle Eocene (approximately 45 Ma), the Neo-Tethys oceanic plate broke off from the Indian continental crust, and asthenospheric mantle upwelling occurred. Qi et al. (2008) [97] first studied Himalayan Eocene granites and proposed that the Dala pluton was formed at the India–Lhasa continental–continental collision stage and originated from material remelting of the middle and lower crusts of the Indian block. Zeng et al. (2011) [10] explained the genesis of Eocene (44–42 Ma) granites in the Yardoï dome and its adjacent area for the first time using the plate fracture model. Ji et al. (2016) [58] identified 45 Ma oceanic island basalt (OIB)-type gabbro, which constrained the fracture time of the Neo-Tethys plate in the central and eastern orogenic belt regions. Immediately, a large amount of magmatic activity occurred in the northern Himalayas from 45 to 40 Ma, forming Eocene medium-basic dikes [58,98,99], adakitic rocks [10,21–23] and leucogranites [11,24,100]. Aikman et al. (2008) [101] reported that the formation of the Dala pluton occurred later than the crustal thickening process of the northern Himalayan fold belt. Zeng et al. (2011) [10] and Xie et al. (2010) [15] proposed that the Dala pluton shares the geochemical characteristics of adakitic rocks, which originated from dehydration partial melting of amphibolite under the thickened crust. Later studies confirmed this view and determined that the formation time of partial melting granite related to the thickened crust was 43 Ma [22,25].

Combined with previous studies, we propose that between 55 and 45 Ma, the front of the Indian passive continental margin collided with the Lhasa block, resulting in medium- to high-pressure metamorphism and partial melting of the middle–lower crust. The upper crust (the northern Himalayas) was compressed to form a fold–fault zone, and a small amount of leucogranite and adakitic rock emerged from 49–45 Ma (Figure 16a). At approximately 45 Ma, the Neo-Tethys oceanic plate subducted to a certain depth broke off from the Indian continental plate, and asthenospheric upwelling occurred. From 45 to 40 Ma, due to the detachment of the Neo-Tethys oceanic crust plate, the northern Himalayas experienced short-term extensional extension. The early partial melting magma in the high-temperature and high-pressure environment of the middle–lower crust invaded the northern Himalayas from 45 to 40 Ma to form many Eocene adakitic rocks (Figure 16a). It is speculated that the angle of the subducting plate changed from high to low angles from 39 to 29 Ma. During this period, the Himalayas were dominated by continuous crustal thickening [33]. Due to the transformation of the tectonic environment, only a small amount of leucogranite was exposed from 37 to 35 Ma (Figure 16b).

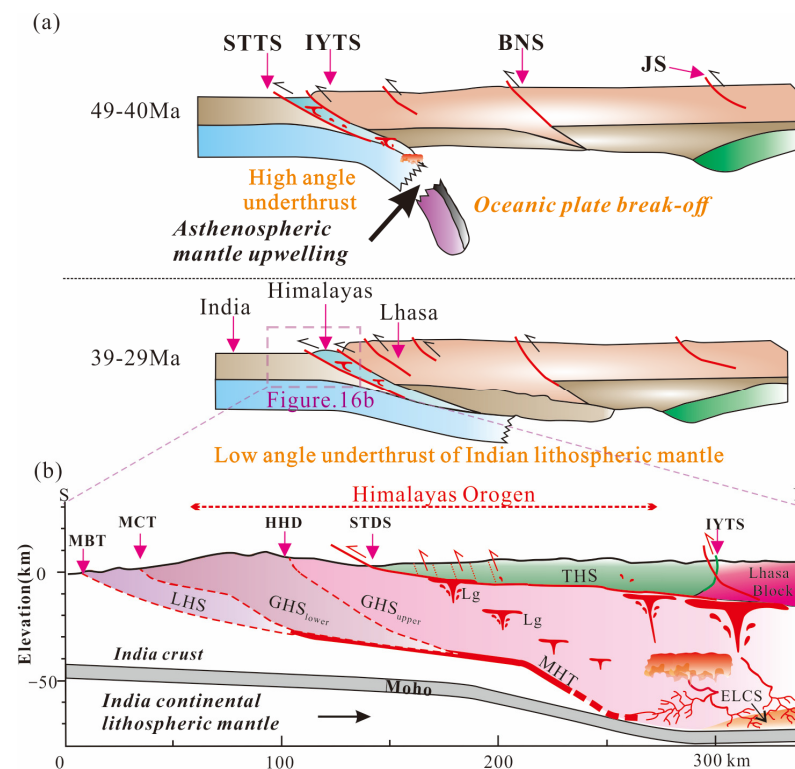


**Figure 16.** Eocene tectonic evolution model for the Himalayan region. (a) From 49 to 40 Ma, break-off occurred between the Indian continental lithosphere and the Neo-Tethys oceanic slab and the Indian lithosphere subducted under the Lhasa Block at a low angle during 39–29 Ma. (b) Structural profile of the Himalayan fault–fold belt (modified from Cao and Pei et al., 2023a [7]; Cao et al., 2022 [6]).

## 7. Conclusions

1. Liemai muscovite granites were emplaced at ca. 42 Ma and are characterized by peraluminous features, high Sr/Y and La/Yb ratios, and low Y and Yb concentrations, suggesting an adakitic affinity, similar to that of the granites formed during the same period in adjacent areas (Yalaxiangbo, Dala, Quedang, etc.).
2. The Eocene adakitic rock is the result of the partial melting of metapelite dominated by amphibolite in the deep crust under high temperature and high pressure in the crustal thickening process. The leucogranite is the result of the continuous fractional crystallization of plagioclase against the same geological background in a relatively shallow low-temperature and low-pressure environment.

3. Eocene adakitic rocks only developed significantly during the early Eocene (47–40 Ma) and were obviously stunted from 40 to 35 Ma, which may represent a tectonic transition period. Leucogranites were actively formed throughout the Eocene, and there was a clear episodic growth trend from 51 to 40 Ma. The peak age trough between 40 and 37 Ma may have been influenced by the same tectonic event as that impacting the adakitic rocks.
4. It is proposed that the transition from a high- to low-angle subduction plate may affect deep crustal diagenesis conditions such as temperature and pressure, resulting in differences in the spatial and temporal distributions of Eocene adakitic rocks and leucogranites.

**Supplementary Materials:** The following supporting information can be downloaded at: <https://www.mdpi.com/article/10.3390/min13091204/s1>, Table S1: Age summary of Eocene magmatic rocks in the Himalayas; Table S2: Zircon U–Pb data of the magmatic zircons from the Liemai muscovite granites; Table S3: Zircon Hf isotope data from magmatic zircons in the Liemai muscovite granites samples from the eastern of Tethyan Himalaya; Table S4: U–Th–Pb dating results for monazite from the Liemai muscovite granites; Table S5: REE and trace elements for monazite from the Liemai muscovite granites; Table S6: Major element, Trace elements and REE abundance of the Liemai muscovite granites, eastern of the Tethyan Himalaya; Table S7: In situ Nd isotopes date results for monazite from the Liemai muscovite granites; Table S8: In situ plagioclase Sr isotopes for the Liemai muscovite granites in the eastern Tethyan Himalaya; Table S9: Summary of the whole-rock Pb isotopes for the Liemai muscovite granites in the eastern Tethyan Himalaya; Table S10: Major element, Trace elements and REE abundance of the Himalayan Eocene Adakitic rocks; Table S11: Major element, Trace elements and REE abundance of the Himalayan Eocene Leucogranite; Table S12: Zircon, Monazite, Titanite U–Pb ages and Hf isotopic data of Eocene Magmatic rocks in the Himalayas; Table S13: Sr–Nd–Pb isotope statistics of the Eocene Adakitic rocks and Leucogranite in the Himalayas.

**Author Contributions:** Conceptualization, H.L. and H.C.; methodology, X.Z.; validation, Y.L.; formal analysis, H.C.; investigation, H.L.; resources, H.C.; data curation, H.L.; writing—original draft preparation, H.L.; writing—review and editing, W.L. and H.C.; supervision, K.Z., X.L., L.D. and K.G.; funding acquisition, W.L. All authors have read and agreed to the published version of the manuscript.

**Funding:** This research was financially supported in part by the National Key Research and Development Program of China (Grant Nos: 2021YFC2901803); the National Natural Science Foundation of China (Grant Nos: 92055314); and the International Geoscience Programme (IGCP-741). The funder is the project leader named Li Wenchang.

**Data Availability Statement:** Not applicable.

**Acknowledgments:** Thanks to Dai Zuowen of the University of Science and Technology Beijing for valuable suggestions on this article. Thanks to Yang Lei from Chengdu University of Technology for sincere advice on data processing. Finally, we are grateful to the editor and the three reviewers.

**Conflicts of Interest:** The authors declare no conflict of interest.

## References

1. Le Fort, P.; Cuney, M.; Deniel, C.; Francelanord, C.; Sheppard, S.M.F.; Upreti, B.N.; Vidal, P. Crustal generation of the Himalayan leucogranites. *Tectonophysics* **1987**, *134*, 39–57. [[CrossRef](#)]
2. Hodges, K.V. Tectonics of the Himalaya and southern Tibet from two perspectives. *Geol. Soc. Am. Bull.* **2000**, *112*, 324–350. [[CrossRef](#)]
3. Mo, X.X.; Hou, Z.Q.; Niu, Y.L.; Dong, G.C.; Qu, X.M.; Zhao, Z.D.; Yang, Z. Mantle contributions to crustal thickening during continental collision: Evidence from Cenozoic igneous rocks in southern Tibet. *Lithos* **2007**, *96*, 225–242. [[CrossRef](#)]
4. Hou, Z.; Duan, L.; Lu, Y.; Zheng, Y.; Zhu, D.; Yang, Z.; Yang, Z.; Wang, B.; Pei, Y.; Zhao, Z.; et al. Lithospheric architecture of the Lhasa terrane and its control on ore deposits in the Himalayan–Tibetan orogen. *Econ. Geol.* **2015**, *110*, 1541–1575. [[CrossRef](#)]
5. Wu, F.Y.; Liu, X.C.; Liu, Z.C.; Wang, R.C.; Xie, L.; Wang, J.M.; Ji, W.Q.; Yang, L.; Liu, C.; Khanal, G.P.; et al. Highly fractionated Himalayan leucogranites and associated rare-metal mineralization. *Lithos* **2020**, *352–353*, 105319. [[CrossRef](#)]

6. Cao, H.W.; Pei, Q.M.; Santosh, M.; Li, G.M.; Zhang, L.K.; Zhang, X.F.; Zhang, Y.H.; Zou, H.; Dai, Z.W.; Lin, B.; et al. Himalayan leucogranites: A review of geochemical and isotopic characteristics, timing of formation, Genesis, and rare metal mineralization. *Earth-Sci. Rev.* **2022**, *234*, 104229. [[CrossRef](#)]
7. Cao, H.W.; Pei, Q.M.; Yu, X.; Santosh, M.; Li, G.M.; Zhang, L.K.; Dong, L.; Gao, K.; Dai, Z.W.; Ai, J.B.; et al. Discovery of the large-scale Eocene Xiwu Pb-Zn-Ag deposit in the Tethyan Himalaya: Geochronology, geochemistry, and C-H-O-S-Pb-Sr-Nd isotopes. *Gondwana Res.* **2023**, *124*, 165–187. [[CrossRef](#)]
8. Cao, H.W.; Pei, Q.M.; Yu, X.; Cao, A.B.; Chen, Y.; Liu, H.; Zhang, K.; Liu, X.; Zhang, X.F. The long-lived partial melting of the greater Himalayas in southern Tibet, constraints from the Miocene Gyirong anatectic pegmatite and its prospecting potential for rare element minerals. *China Geol.* **2023**, *6*, 303–321.
9. Cao, H.W.; Tang, L.; Yang, C.X.; Santosh, M. Advances in metallogeny and tectonics of the Eastern Tethyan Realm: Introduction. *Geol. J.* **2023**, *58*, 2859–2864. [[CrossRef](#)]
10. Zeng, L.S.; Gao, L.E.; Xie, K.J.; Jing, L.Z. Mid-Eocene high Sr/Y granites in the Northern Himalayan Gneiss Domes: Melting thickened lower continental crust. *Earth Planet. Sci. Lett.* **2011**, *303*, 251–266. [[CrossRef](#)]
11. Zeng, L.S.; Gao, L.E.; Tang, S.H.; Hou, K.J.; Guo, C.L.; Hu, G.Y. Eocene magmatism in the tethyan Himalaya, southern Tibet. *Geol. Soc. Lond. Spec. Publ.* **2014**, *412*, 287–316. [[CrossRef](#)]
12. Liu, Z.C.; Wu, F.Y.; Qiu, Z.L.; Wang, J.G.; Liu, X.C.; Ji, W.Q.; Liu, C.Z. Leucogranite geochronological constraints on the termination of the South Tibetan Detachment in eastern Himalaya. *Tectonophysics* **2017**, *721*, 106–122. [[CrossRef](#)]
13. Hu, F.; Ducea, M.N.; Liu, S.; Chapman, J.B. Quantifying crustal thickness in continental collisional belts: Global perspective and a geologic application. *Sci. Rep.* **2017**, *7*, 7058. [[CrossRef](#)]
14. Hu, F.; Wu, F.; Chapman, J.B.; Ducea, M.N.; Ji, W.; Liu, S. Quantitatively tracking the elevation of the Tibetan Plateau since the cretaceous: Insights from whole-rock Sr/Y and La/Yb ratios. *Geophys. Res. Lett.* **2020**, *47*, e2020GL089202. [[CrossRef](#)]
15. Xie, K.J.; Zeng, L.S.; Gao, L.E. Late-Eocene Dala adakitic granite, southern Tibet and geological implications. *Acta Petrol. Sin.* **2010**, *26*, 1016–1026.
16. Aikman, A.B.; Harrison, T.M.; Hermann, J. Age and thermal history of Eo- and Neohimalayan granitoids, Eastern Himalaya. *J. Asian Earth Sci.* **2012**, *51*, 85–97. [[CrossRef](#)]
17. Gao, L.E.; Zeng, L.S.; Asimow, P.D. Contrasting geochemical signatures of fluid-absent versus fluid-fluxed melting of muscovite in metasedimentary sources: The Himalayan leucogranites. *Geology* **2017**, *45*, 39–42. [[CrossRef](#)]
18. Lin, C.; Zhang, J.; Wang, X.; Huang, T.; Zhang, B.; Fan, Y. Himalayan Miocene adakitic rocks, a case study of the Mayum pluton: Insights into geodynamic processes within the subducted Indian continental lithosphere and Himalayan mid-Miocene tectonic regime transition. *GSA Bull.* **2021**, *133*, 591–611. [[CrossRef](#)]
19. Gao, P.; Zheng, Y.F.; Mayne, M.J.; Zhao, Z.F. Miocene high-temperature leucogranite magmatism in the Himalayan orogen. *GSA Bull.* **2021a**, *133*, 679–690. [[CrossRef](#)]
20. Gao, P.; Zheng, Y.F.; Yakymchuk, C.; Zhao, Z.F.; Meng, Z.Y. The effects of source mixing and fractional crystallization on the composition of Eocene granites in the Himalayan orogen. *J. Petrol.* **2021b**, *62*, egab037. [[CrossRef](#)]
21. Dai, Z.W.; Yang, Z.M.; Li, G.M.; Xie, Y.L.; Dong, L.; Gao, K.; Cao, H.W. Partial melting of amphibolitic lower crust and subsequent melt-crystal separation for generation of the Early Eocene magmatism in eastern Himalaya. *Front. Earth Sci.* **2023**, *10*, 1104197. [[CrossRef](#)]
22. Dai, Z.W.; Dong, L.; Li, G.M.; Huizenga, J.M.; Ding, J.; Zhang, L.K.; Huang, Y.; Cao, H.; Lu, L.; Yan, G. Crustal thickening prior to 43 Ma in the Himalaya: Evidence from lower crust-derived adakitic magmatism in Dala, eastern tethyan Himalaya, Tibet. *Geol. J.* **2020**, *55*, 4021–4046. [[CrossRef](#)]
23. Hou, Z.Q.; Zheng, Y.C.; Zeng, L.S.; Gao, L.E.; Huang, K.X.; Li, W.; Li, Q.Y.; Fu, Q.; Liang, W.; Sun, Q.Z. Eocene–Oligocene granitoids in southern Tibet: Constraints on crustal anatexis and tectonic evolution of the Himalayan orogen. *Earth Planet. Sci. Lett.* **2012**, *349*, 38–52. [[CrossRef](#)]
24. Cao, H.W.; Li, G.M.; Zhang, L.K.; Dong, L.; Gao, K.; Dai, Z.W. Monazite U-Th-Pb age of Liemai Eocene granites in the southern Tibet and its geological implications. *Sediment. Geol. Tethyan Geol.* **2020**, *40*, 31–42, (In Chinese with English Abstract).
25. Tian, L.M.; Wang, L.Y.; Zheng, H.T.; Yang, B. Eocene magmatism from the Liemai intrusion in the eastern tethyan Himalayan belt and tectonic implications. *Geol. Mag.* **2017**, *156*, 510–524. [[CrossRef](#)]
26. He, S.X.; Liu, X.C.; Yang, L.; Wang, J.M.; Hu, F.Y.; Wu, F.Y. Multistage magmatism recorded in a single gneiss dome: Insights from the Lhagoi Kangri leucogranites, Himalayan orogen. *Lithos* **2021**, *398–399*, 106222. [[CrossRef](#)]
27. Lin, C.; Zhang, J.; Wang, X.; Putthapiban, P.; Zhang, B.; Huang, T. Oligocene initiation of the South Tibetan Detachment System: Constraints from syn-tectonic leucogranites in the Kampa Dome, Northern Himalaya. *Lithos* **2020**, *354–355*, 105332. [[CrossRef](#)]
28. Wang, Y.; Zeng, L.; Gao, L.E.; Chen, Z.; Li, S. Eocene thickening without extra heat in a collisional orogenic belt: A record from Eocene metamorphism in mafic dike swarms within the Tethyan Himalaya, southern Tibet. *GSA Bull.* **2022**, *134*, 1217–1230. [[CrossRef](#)]
29. Liu, X.C.; Wu, F.Y.; Yu, L.J.; Liu, Z.C.; Ji, W.Q.; Wang, J.G. Emplacement age of leucogranite in the Kampa Dome, southern Tibet. *Tectonophysics* **2016**, *667*, 163–175. [[CrossRef](#)]
30. Zeng, L.S.; Liu, J.; Gao, L.E.; Xie, K.J.; Wen, L. Early Oligocene anatexis in the Yardoi gneiss dome, southern Tibet and geological implications. *Chin. Sci. Bull.* **2009**, *54*, 104–112. [[CrossRef](#)]

31. Tian, S.H.; Hou, Z.Q.; Mo, X.X.; Tian, Y.H.; Zhao, Y.; Hou, K.J.; Yang, Z.S.; Hu, W.J.; Li, X.F.; Zhang, Y.J. Lithium isotopic evidence for subduction of the Indian lower crust beneath southern Tibet. *Gondwana Res.* **2020**, *77*, 168–183. [[CrossRef](#)]
32. Tian, S.H.; Zhao, Y.; Hou, Z.Q.; Tian, Y.H.; Hou, K.J.; Li, X.F.; Yang, Z.S.; Hu, W.J.; Mo, X.X.; Zheng, Y.C. Lithium isotopic composition and concentration of Himalayan leucogranites and the Indian lower continental crust. *Lithos* **2017**, *284–285*, 416–428. [[CrossRef](#)]
33. Kapp, P.; Decelles, P.G. Mesozoic-Cenozoic geological evolution of the Himalayan-Tibetan orogen and working tectonic hypotheses. *Am. J. Sci.* **2019**, *319*, 159–254. [[CrossRef](#)]
34. Zhang, K.J.; Zhang, Y.X.; Tang, X.C.; Xia, B. Late Mesozoic tectonic evolution and growth of the Tibetan plateau prior to the Indo-Asian collision. *Earth Sci. Rev.* **2012**, *114*, 236–249. [[CrossRef](#)]
35. Yin, A. Cenozoic tectonic evolution of the Himalayan orogen as constrained by along-strike variation of variation of structural geometry, exhumation history, and foreland sedimentation. *Earth Sci. Rev.* **2006**, *76*, 1–131. [[CrossRef](#)]
36. Jessup, M.J.; Langille, J.M.; Diedesch, T.F.; Cottle, J.M. Gneiss Dome Formation in the Himalaya and southern Tibet. *Geol. Soc. Lond. Spec. Publ.* **2019**, *483*, 401–422. [[CrossRef](#)]
37. Cao, H.W.; Huang, Y.; Li, G.M.; Zhang, L.K.; Wu, J.Y.; Dong, L.; Dai, Z.W.; Lu, L. Late Triassic sedimentary records in the northern Tethyan Himalaya: Tectonic link with Greater India. *Geosci. Front.* **2018**, *9*, 273–291. [[CrossRef](#)]
38. Kohn, M.J. Himalayan Metamorphism and its Tectonic Implications. *Annu. Rev. Earth Planet. Sci.* **2014**, *42*, 381–419. [[CrossRef](#)]
39. Kumar, S.; Pundir, S. Tectono-magmatic evolution of granitoids in the Himalaya and Trans-Himalaya. *Himal. Geol.* **2021**, *42*, 213–246.
40. Zong, K.Q.; Liu, Y.S.; Gao, C.G.; Hu, Z.C.; Gao, S.; Gong, H.J. In situ U-Pb dating and trace element analysis of zircons in thin sections of eclogite: Refining constraints on the ultra-high pressure metamorphism of the Sulu terrane, China. *Chem. Geol.* **2010**, *269*, 237–251. [[CrossRef](#)]
41. Liu, Y.S.; Hu, Z.C.; Gao, S.; Günther, D.; Xu, J.; Gao, C.G.; Chen, H.H. In situ analysis of major and trace elements of anhydrous minerals by LA-ICP-MS without applying an internal standard. *Chem. Geol.* **2008**, *257*, 34–43. [[CrossRef](#)]
42. Liu, Y.S.; Gao, S.; Hu, Z.C.; Gao, C.G.; Zong, K.Q.; Wang, D.B. Continental and oceanic crust recycling-induced melt-peridotite interactions in the Trans-North China Orogen: U-Pb dating, Hf isotopes and trace elements in zircons of mantle xenoliths. *J. Petrol.* **2010**, *51*, 537–571. [[CrossRef](#)]
43. Ludwig, K.R. *ISOPLOT 3.00: A Geochronological Toolkit for Microsoft Excel*; Berkeley Geochronology Center: Berkeley, CA, USA, 2003; 39p.
44. Hu, Z.C.; Zhang, W.; Liu, Y.S.; Gao, S.; Li, M.; Zong, K.Q.; Chen, H.H.; Hu, S.H. “Wave” signal-smoothing and mercury-removing device for laser ablation quadrupole and multiple collector ICPMS analysis: Application to lead isotope analysis. *Anal. Chem.* **2015**, *87*, 1152–1157. [[CrossRef](#)]
45. Zhang, W.; Hu, Z.; Liu, Y.; Wu, T.; Deng, X.; Guo, J.; Zhao, H. Improved in situ Sr isotopic analysis by a 257 nm femtosecond laser in combination with the addition of nitrogen for geological minerals. *Chem. Geol.* **2018**, *479*, 10–21. [[CrossRef](#)]
46. Tong, X.R.; Liu, Y.S.; Hu, Z.C.; Chen, H.H.; Zhou, L.; Hu, Q.H.; Xu, R.; Deng, L.X.; Chen, C.F.; Yang, L.; et al. Accurate determination of Sr isotopic compositions in clinopyroxene and silicate glasses by LA-MC-ICP-MS. *Geostand. Geoanal. Res.* **2016**, *40*, 85–99. [[CrossRef](#)]
47. Xu, L.; Hu, Z.C.; Zhang, W.; Yang, L.; Liu, Y.S.; Gao, S. In situ Nd isotope analyses in geological materials with signal enhancement and non-linear mass dependent fractionation reduction using laser ablation MC-ICP-MS. *J. Anal. At. Spectrom.* **2015**, *30*, 232–244. [[CrossRef](#)]
48. Russell, W.A.; Papanastassiou, D.A.; Tombrello, T.A. Ca isotope fractionation on the earth and other solar system materials. *Geochim. Cosmochim. Acta* **1978**, *42*, 1075–1090. [[CrossRef](#)]
49. Gao, J.F.; Lu, J.J.; Lai, M.Y.; Lin, Y.P.; Pu, W. Analysis of trace elements in rock samples using HR-ICPMS. *J. Nanjing Univ. Nat. Sci.* **2003**, *39*, 844–850, (In Chinese with English Abstract).
50. Middlemost, E.A.K. Naming materials in the magma/igneous rock system. *Earth-Sci. Rev.* **1994**, *37*, 215–224. [[CrossRef](#)]
51. Maniar, P.D.; Piccoli, P.M. Tectonic discrimination of granitoids. *Geol. Soc. Am. Bull.* **1989**, *101*, 635–643. [[CrossRef](#)]
52. Peccerillo, A.; Taylor, S.R. Geochemistry of eocene calc-alkaline volcanic rocks from the Kastamonu area, Northern Turkey. *Contrib. Mineral. Petrol.* **1976**, *58*, 63–81. [[CrossRef](#)]
53. Watson, E.B.; Harrison, T.M. Zircon saturation revisited: Temperature and composition effects in a variety of crustal magma types. *Earth Planet. Sci. Lett.* **1983**, *64*, 295–304. [[CrossRef](#)]
54. Liu, Z.C.; Wu, F.Y.; Ji, W.Q.; Wang, J.G.; Liu, C.Z. Petrogenesis of the Ramba leucogranite in the Tethyan Himalaya and constraints on the channel flow model. *Lithos* **2014**, *208–209*, 118–136. [[CrossRef](#)]
55. Li, Z.L. *Geochronology, Geochemistry and Geodynamic Significance of the Dala Two-Mica Granite in Tethyan Himalaya, Tibet*; China University of Geosciences: Beijing, China, 2016. (In Chinese with English Abstract)
56. Yang, J.Y.; Fei, G.C.; Ding, F.; Zhao, D.K.; Deng, Y.; Gao, J.G.; Shi, S. The geochemical characteristics and geological significance of the monzogranite in rongboza, nagarze, Tibet. *J. Mineral. Petrol.* **2019**, 69–77.
57. Ji, W.Q.; Wu, F.Y.; Wang, J.M.; Liu, X.C.; Liu, Z.C.; Zhang, Z.; Cao, W.; Wang, J.G.; Zhang, C. Early evolution of Himalayan orogenic belt and generation of middle Eocene magmatism: Constraint from Haweng Granodiorite Porphyry in the Tethyan Himalaya. *Front. Earth Sci.* **2020**, *8*, 236. [[CrossRef](#)]

58. Ji, W.Q.; Wu, F.Y.; Chung, S.L.; Wang, X.C.; Liu, C.Z.; Li, Q.L.; Liu, Z.C.; Liu, X.C.; Wang, J.G. Eocene Neo-Tethyan slab breakoff constrained by 45 Ma oceanic island basalt–type magmatism in southern Tibet. *Geology* **2016**, *44*, 283–286. [[CrossRef](#)]
59. Bian, Q.T.; Ding, L. Discovery of the Zhegucuo au (As)-bearing fine granular quartz diorite in the eastern Tethyan Himalayan Belt and its significance. *Acta Petrol. Sin.* **2006**, *22*, 977–988, (In Chinese with English Abstract).
60. Larson, K.P.; Godin, L.; Davis, W.J.; Davis, D.W. Out-of-sequence deformation and expansion of the Himalayan orogenic wedge: Insight from the Changgo culmination, south central Tibet. *Tectonics* **2010**, *29*, TC4013. [[CrossRef](#)]
61. Liu, Z.C.; Wu, F.Y.; Ding, L.; Liu, X.C.; Wang, J.G.; Ji, W.Q. Highly fractionated Late Eocene (~35 Ma) leucogranite in the Xiaru Dome, Tethyan Himalaya, South Tibet. *Lithos* **2016**, *240–243*, 337–354. [[CrossRef](#)]
62. Zhou, Q.; Li, W.C.; Wang, G.C.; Liu, Z.; Lai, Y.; Huang, J.H.; Yan, G.Q.; Zhang, Q.C. Chemical and boron isotopic composition of tourmaline from the Conadong leucogranite pegmatite system in South Tibet. *Lithos* **2019**, *326–327*, 529–539. [[CrossRef](#)]
63. Defant, M.J.; Drummond, M.S. Derivation of some modern arc magmas by melting of young subducted lithosphere. *Nature* **1990**, *347*, 662–665. [[CrossRef](#)]
64. Skjerlie, K.P.; Johnston, A.D. Vapour-absent melting from 10 to 20 kbar of crustal rocks that contain multiple hydrous phases: Implications for anatexis in the deep to very deep continental crust and active continental margins. *J. Petrol.* **1996**, *37*, 661–691. [[CrossRef](#)]
65. Lu, L.; Zhang, K.J.; Jin, X.; Zeng, L.; Yan, L.L.; Santosh, M. Crustal thickening of central Tibet prior to the Indo–Asian collision: Evidence from petrology, geochronology, geochemistry and Sr–Nd–Hf isotopes on K-rich charnockite–granite suite in eastern Qiangtang. *J. Petrol.* **2019**, *60*, 827–854. [[CrossRef](#)]
66. Patiño Douce, A.E.; Beard, J.S. Dehydration-melting of biotite gneiss and quartz amphibolite from 3 to 15 kbar. *J. Petrol.* **1995**, *36*, 707–738. [[CrossRef](#)]
67. Sylvester, P.J. Post-collisional strongly peraluminous granites. *Lithos* **1998**, *45*, 29–44. [[CrossRef](#)]
68. Yang, X.M. Estimation of crystallization pressure of granite intrusions. *Lithos* **2017**, *286–287*, 324–329. [[CrossRef](#)]
69. Yang, L.; Calvin, F.M.; Wu, F.Y. Estimating crystallization pressure of peraluminous melts: An experimentally based empirical approach. *Contrib. Mineral. Petrol.* **2022**, *177*, 78. [[CrossRef](#)]
70. Breiter, K.; Škoda, R. Zircon and whole-rock Zr/Hf ratios as markers of the evolution of granitic magmas: Examples from the Teplice caldera (Czech Republic/Germany). *Mineral. Petrol.* **2017**, *111*, 435–457. [[CrossRef](#)]
71. Štípská, P.; Závada, P.; Collett, S.; Kylander-Clark, A.R.; Hacker, B.R.; Tabaud, A.S.; Racek, M. Eocene migmatite formation and diachronous burial revealed by petrochronology in NW Himalaya, Zaskar. *J. Metamorph. Geol.* **2020**, *38*, 655–691. [[CrossRef](#)]
72. Kawabata, R.; Imayama, T.; Bose, N.; Yi, K.; Kouketsu, Y. Tectonic discontinuity, partial melting and exhumation in the Garhwal Himalaya (Northwest India): Constrains from spatial and temporal pressure-temperature conditions along the Bhagirathi valley. *Lithos* **2021**, *404–405*, 106488. [[CrossRef](#)]
73. Dai, Z.W.; Li, G.M.; Ding, J.; Li, Y.X.; Dong, L.; Huang, Y.; Cao, H.W. Late Cretaceous Adakite in Nuri Area, Tibet: Products of ridge subduction. *Earth Sci.* **2018**, *43*, 2727–2741, (In Chinese with English Abstract).
74. Defant, M.J.; Drummond, M.S. Mount St. Helens: Potential example of the partial melting of the subducted lithosphere in a volcanic arc. *Geology* **1993**, *21*, 547–550. [[CrossRef](#)]
75. Karsli, O.; Dokuz, A.; Uysal, İ.; Aydin, F.; Kandemir, R.; Wijbrans, J. Generation of the Early Cenozoic adakitic volcanism by partial melting of mafic lower crust, Eastern Turkey: Implications for crustal thickening to delamination. *Lithos* **2010**, *114*, 109–120. [[CrossRef](#)]
76. Lai, S.C.; Qin, J.F. Adakitic rocks derived from the partial melting of subducted continental crust: Evidence from the Eocene volcanic rocks in the northern Qiangtang block. *Gondwana Res.* **2013**, *23*, 812–824. [[CrossRef](#)]
77. Yu, H.X.; Chen, J.L.; Xu, J.F.; Wang, B.; Wu, J.B.; Liang, H.Y. Geochemistry and origin of Late Cretaceous (similar to 90Ma) ore-bearing porphyry of Balazha in mid-northern Lhasa terrane, Tibet. *Acta Petrol. Sin.* **2011**, *27*, 2011–2022. (In Chinese with English Abstract)
78. Zeng, L.S.; Liu, J.; Hou, Z.Q.; Gao, L.E.; Xie, K.J. *Fluxed-Melting of Shallow and Hot High-Grade Metamorphic Rocks in the Namcha Barwa Massif: A New Mechanism for the Generation of Adakitic Melts*; EOS, Translator; AGU: Washington, DC, USA, 2008; Volume 89.
79. Guo, Z.F.; Wilson, M.; Liu, J.Q. Post-collisional adakites in south Tibet: Products of partial melting of subduction-modified lower crust. *Lithos* **2007**, *96*, 205–224. [[CrossRef](#)]
80. Castillo, P.R. Adakite petrogenesis. *Lithos* **2012**, *134–135*, 304–316. [[CrossRef](#)]
81. Macpherson, C.G.; Dreher, S.T.; Thirlwall, M.F. Adakites without slab melting: High pressure differentiation of island arc magma, Mindanao, the Philippines. *Earth Planet. Sci. Lett.* **2006**, *243*, 581–593. [[CrossRef](#)]
82. Castillo, P.R.; Janney, P.E.; Solidum, R.U. Petrology and geochemistry of Camiguin Island, southern Philippines: Insights to the source of adakites and other lavas in a complex arc setting. *Contrib. Mineral. Petrol.* **1999**, *134*, 33–51. [[CrossRef](#)]
83. Hastie, A.R.; Kerr, A.C.; Pearce, J.A.; Mitchell, S.F. Classification of altered volcanic island arc rocks using immobile trace elements: Development of the Th–Co discrimination diagram. *J. Petrol.* **2007**, *48*, 2341–2357. [[CrossRef](#)]
84. Ding, H.X.; Hou, Q.Y.; Zhang, Z.M. Petrogenesis and tectonic significance of the Eocene adakite-like rocks in western Yunnan, southeastern Tibetan Plateau. *Lithos* **2016**, *245*, 161–173. [[CrossRef](#)]
85. Green, H.T. Anatexis of mafic crust and high pressure crystallization of andesite. In *Andesites: Orogenic Andesites and Related Rocks*; Thorpe, R.S., Ed.; John Wiley and Sons: New York, NY, USA, 1982; pp. 465–487.

86. Rapp, R.P.; Shimizu, N.; Norman, M.; Applegate, G. Reaction between slab-derived melts and peridotite in the mantle wedge: Experimental constraints at 3.8 GPa. *Chem. Geol.* **1999**, *160*, 335–356. [[CrossRef](#)]
87. Xiong, X.L.; Liu, X.C.; Zhu, Z.M.; Li, Y.; Xiao, W.S.; Song, M.S.; Wu, J.H. Adakitic rocks and destruction of the North China Craton: Evidence from experimental petrology and geochemistry. *Sci. China Earth Sci.* **2011**, *54*, 858–870. [[CrossRef](#)]
88. Chapman, J.B.; Ducea, M.N.; DeCelles, P.G.; Profeta, L. Tracking changes in crustal thickness during orogenic evolution with Sr/Y: An example from the North American Cordillera. *Geology* **2015**, *43*, 919–922. [[CrossRef](#)]
89. Zhang, Q.; Wang, Y.; Li, C.D.; Jin, W.J.; Jia, X.Q. A granite classification based on pressures. *Geol. Bull. China* **2006**, *25*, 1274–1278.
90. Zeng, L.S.; Asimow, P.; Saleeby, J.B. Coupling of anatexis reactions and dissolution of accessory phases and the Sr and Nd isotope systematics of anatexis melts from a metasedimentary source. *Geochim. Cosmochim. Acta* **2005**, *69*, 3671–3682. [[CrossRef](#)]
91. Ayres, M.; Harris, N.; Vance, D. Possible constraints on anatexis melt residence times from accessory mineral dissolution rates: An example from Himalayan leucogranites. *Mineral. Mag.* **1997**, *61*, 29–36. [[CrossRef](#)]
92. Watt, G.R.; Harley, S.L. Accessory phase controls on the geochemistry of crustal melts and restites produced during water-undersaturated partial melting. *Contrib. Mineral. Petrol.* **1993**, *114*, 550–566. [[CrossRef](#)]
93. Zhang, Z.M.; Ding, H.X.; Dong, X.; Tian, Z.L. Two contrasting eclogite types in the Himalayan Orogen and differential subduction of Indian continent. *Earth Sci. Rev.* **2019**, *44*, 1602–1619. (In Chinese with English Abstract)
94. Montomali, C.; Iaccarino, S.; Antolin, B.; Appel, E.; Carosi, R.; Dunkl, I.; Lin, D.; Visonà, D. Tectonometamorphic evolution of the Tethyan Sedimentary Sequence (Himalayas, SE Tibet). *Ital. J. Geosci.* **2017**, *136*, 73–88. [[CrossRef](#)]
95. Gao, L.E.; Zeng, L.S.; Xie, K.J. Eocene high grade metamorphism and crustal anatexis in the North Himalaya Gneiss Domes, Southern Tibet. *Chin. Sci. Bull.* **2012**, *57*, 639–650. [[CrossRef](#)]
96. Rehman, H.U. Geochronological enigma of the HP-UHP rocks in the Himalayan orogen. *Geol. Soc. Lond. Spec. Publ.* **2019**, *474*, 183–207. [[CrossRef](#)]
97. Qi, X.X.; Zeng, L.S.; Meng, X.J.; Xu, Z.Q.; Li, T.F. Zircon SHRIMP U-Pb dating for Dala granite in the Tethyan Himalaya and its geological implication. *Acta Petrol. Sin.* **2008**, *24*, 1501–1508. (In Chinese with English Abstract)
98. Wu, Z.H.; Ye, P.S.; Wu, Z.H.; Zhao, Z. LA-ICP-MS zircon U-Pb ages of tectonic-thermal events in the Yalaxiangbo dome of Tethys Himalayan belt. *Geol. Bull. China* **2014**, *33*, 595–605. (In Chinese with English abstract)
99. Ding, L.; Kapp, P.; Wan, X.Q. Paleocene–Eocene record of ophiolite obduction and initial India-Asia collision, south central Tibet. *Tectonics* **2005**, *24*, TC3001. [[CrossRef](#)]
100. Liu, Z.C. Geochronology and Petrogenesis of the Ramba Leucogranite, Tethyan Himalaya, Tibet. Ph.D. Thesis, University of China Academy of Sciences, Beijing, China, 2013. (In Chinese with English abstract)
101. Aikman, A.B.; Harrison, T.M.; Lin, D. Evidence for Early (>44 Ma) Crustal Thickening, Tethyan Himalaya, southeastern Tibet. *Earth Planet. Sci. Lett.* **2008**, *274*, 14–23. [[CrossRef](#)]

**Disclaimer/Publisher’s Note:** The statements, opinions and data contained in all publications are solely those of the individual author(s) and contributor(s) and not of MDPI and/or the editor(s). MDPI and/or the editor(s) disclaim responsibility for any injury to people or property resulting from any ideas, methods, instructions or products referred to in the content.